

Chapter 2

Remote Sensing and Modelling of Atmospheric Chemistry and Sea Ice Parameters

2.1 NO₂ Pollution Trends Over Megacities 1996–2010 from Combined Multiple Satellite Data Sets

Andreas Hilboll (✉), Andreas Richter and John P. Burrows

Institute of Environmental Physics, University of Bremen, Germany
e-mail: hilboll@iup.physics.uni-bremen.de

Abstract Nitrogen oxides ($\text{NO}_x = \text{NO}_2 + \text{NO}$) are air pollutants emerging mainly from fossil fuel combustion, i.e. traffic, power generation, and industry. Apart from being hazardous to human health, they contribute to acid rain and play a major role in tropospheric ozone formation. While NO_x concentrations can most accurately be monitored using ground-based in-situ measurements, remote sensing techniques in general and satellite instruments in particular have proven invaluable to obtain long and consistent time series with global coverage. These data sets facilitate studying the temporal evolution of atmospheric pollutants like NO_2 , as they allow applying identical measurement techniques to all investigated regions, yielding comparable results. In this study, we present an assessment of the evolution of tropospheric NO_2 for the 1996–2010 time period. Satellite measurements from the GOME, SCIAMACHY, OMI, and GOME-2 instruments are used in an ensemble approach to investigate trends in tropospheric NO_2 . The focus is on large urban agglomerations, where air quality is most important for human health. Our findings show generally decreasing NO_2 levels for most urban agglomerations of the developed world, while annual growth rates for developing cities can be as high as 9 % annually.

Keywords Air pollution · Megacities · Trend analysis · Nitrogen dioxide · GOME · SCIAMACHY

2.1.1 Introduction

Since the year 2009, more than half of the Earth's human population is living in cities (United Nations Department of Economic and Social Affairs 2010). This trend of increasing urbanization is particularly pronounced in the developing countries, especially in megacities of 10 million inhabitants and more. Due to the very high population density, energy use, and traffic, these agglomerations are hot-spots in terms of air pollution, having large negative health impacts on an increasing number of people (Smith 1993).

One of the main atmospheric pollutants in a megacity environment is the class of nitrogen oxides ($\text{NO}_x = \text{NO} + \text{NO}_2$). NO_x are formed as NO by the reaction of nitrogen and oxygen atoms, disassociated from their molecular state by the high temperatures found in industrial and traffic combustion processes.¹ In daylight conditions, NO and NO_2 then undergo constant cycling (Seinfeld and Pandis 2006). Due to its relatively short lifetime of several hours to a few days, the natural sources of nitrogen oxides (biomass burning, lightning, soils) account for most tropospheric NO_x in rural areas. They are, however, not relevant in most megacity environments. While NO_2 itself is very poisonous, its impact on human health and the environment is even further augmented by its major role in the formation of tropospheric ozone and, via the formation of nitric acid, as acid rain (Seinfeld and Pandis 2006).

While ground-based in situ instruments have been employed to monitor NO_x concentrations for a long time, NO_2 , among other trace gases, can also be investigated using remote-sensing techniques. As light travels through the atmosphere, it is partly absorbed by trace constituents along the way following the Beer-Lambert law, which allows for using spectroscopic approaches. One example is differential optical absorption spectroscopy (DOAS) (Platt and Stutz 2008), which yields the integrated number of absorber molecules along the average light path through the atmosphere, called the total slant column density. In recent years, such DOAS instruments have been mounted on satellite platforms, granting the advantage of comparable measurement conditions for all locations, global coverage every few days, and reduced biases introduced by the location of possible ground-based measurement stations. On the other hand, satellite measurements suffer from low spatial resolution, often cloudy scenes, and quite high uncertainties, which are due to non-perfect knowledge of the exact light path through the atmosphere.

Since 1995, a total of four satellite-based instruments provides measurements of tropospheric NO_2 by means of DOAS: GOME (Burrows et al. 1999), SCIAM-ACHY (Bovensmann et al. 1999a, b), OMI (Levelt et al. 2006), and GOME-2 (Callies et al. 2000). All instruments fly in near-polar, sun-synchronous orbits,

¹ This process of NO formation is called *Zeldovich mechanism*. While for road transport, it accounts for 90–95 % of all emitted NO, this fraction depends strongly on the fuel type and is considerably lower for, e.g., combustion of coal.

Table 2.1 Key characteristics of the four satellite instruments used in this study

Instrument	Equator crossing	Global coverage (days)	Available period	Pixel (km ²)
GOME	10.30 a.m.	3	1995/10–2003/06	40 × 320
SCIAMACHY	10.00 a.m.	6	2002/08–now	30 × 60
OMI	1.30 p.m.	1	2004/10–now	13 × 24
GOME-2	9.30 a.m.	1.5	2007/01–now	40 × 80

leading to constant local overpass times for all measurements. The distinct characteristics of the four instruments are summarized in Table 2.1.

Combining different instruments’ time series into one consistent trend estimate is challenging, as spatial resolution differences introduce inconsistencies. Previous studies therefore either artificially downgraded the higher-resolved measurements to yield comparable pixel sizes (Konovalov et al. 2010; van der A et al. 2008), or studied large areas, where instrumental differences tend to average out (Richter et al. 2005).

2.1.2 Method

The spectra of backscattered solar radiation as measured by the four instruments GOME, SCIAMACHY, OMI, and GOME-2 are analyzed to derive total slant column densities of NO₂ using the DOAS method (Platt and Stutz 2008). The stratospheric component of the measured signal is subtracted from the total columns using scaled NO₂ fields from the Bremen 3d Chemistry and Transport Model (CTM) (Sinnhuber et al. 2003b, c; Richter et al. 2005). The resulting tropospheric slant columns are then converted to vertical columns using radiative transfer calculations based on climatological data (Nüß 2005; Richter et al. 2005). Finally, a cloud filter based on the FRESCO+ cloud algorithm (Wang et al. 2008) is applied to select only those measurements with less than 20 % cloud cover.

The derived tropospheric vertical column densities (VCD_{trop}) of NO₂ are then binned globally to a 0.125° × 0.125° grid. For each instrument, daily and, subsequently, monthly averages are calculated. For each region of interest, one VCD_{trop} NO₂, denoted by $Y_{(t,i)}$, is then calculated per time t (in years) and satellite instrument i by averaging over all grid cells within the region’s boundaries.

To derive trend estimators for the temporal evolution of the linear and harmonic components of the measured VCD_{trop}, we assume that the measured values consist of a trend and a noise component (Mudelsee 2010):

$$Y(t, i) = X_{trend}(t, i) + S(i) \cdot X_{noise}(t, i) \quad (2.1)$$

Here, $S(i)$ denotes the standard deviation of all $Y_{(t,i)}$ for the given i (as a measure of the instrument’s variability), and the trend component $X_{trend}(t, i)$ is defined by

$$X_{trend}(t, i) = \omega \cdot t + \mu_i + \eta_i \cdot (1 + \xi \cdot t) \cdot \sum_{j=1}^4 (\beta_{1,j} \cdot \sin(2\pi jt + \varphi) + \beta_{2,j} \cdot \cos(2\pi jt + \varphi)) \quad (2.2)$$

ω is the linear annual growth rate, μ_i are the offsets of the linear trend per instrument, $\beta_{k,j}$ are the coefficients of the sine/cosine expansion to model the seasonal cycle, while η_i gives the amplitude of the seasonality, and ξ accounts for a trend in the amplitude of the seasonality.² For ease of notation, we define the parameter vector $\theta = (\omega, \mu_i, \eta_i, \xi, \beta_{k,j}, \varphi)$.

The corresponding trend estimator $\hat{\theta}$ is then calculated by minimizing the sum of the squared noise components using a modified Powell's method (Powell 1964).

2.1.3 Results

When the trend model (1) is fitted to data from large regions such as the central East coast of the USA, the agreement between the different instruments' measurements is expectedly good. This is reflected in the large similarity between the instrument-dependent trend parameters $\hat{\mu}_i$ and $\hat{\eta}_i$, as $\sigma(\hat{\mu}_i)/\hat{\mu}_i = 0.03$ and $\sigma(\hat{\eta}_i)/\hat{\eta}_i = 0.07$. The trend parameters found for this region are $\hat{\omega} = -4.7\%$ per year and $\hat{\xi} = -6.0\%$ per year.³

When applied to data from megacity regions, the differences between the instruments become more apparent. Generally, we find strong decreasing trends in the developed world, while developing megacities show strong increasing trends as expected. In virtually all cases the signs of $\hat{\omega}$ and $\hat{\xi}$ are the same. The magnitude of the harmonic trend estimator $\hat{\xi}$ however varies greatly. While for many regions, $\hat{\omega}$ and $\hat{\xi}$ are similar in magnitude (e.g. Beijing, Hong Kong, New York, Po Valley), very often the harmonic component $\hat{\xi}$ is significantly larger than $\hat{\omega}$, as e.g., in Athens, Baghdad, Barcelona, and Cairo. Of those regions considered in this study, only the BeNeLux region shows no clear change in the seasonality of the measured NO_2 signal.

Many regions do not show large differences between the instruments (e.g. Delhi), while in other regions, these differences are strongly pronounced, as in Tehran (see Fig. 2.1). The linear and harmonic components $\hat{\omega}$ and $\hat{\xi}$ for some selected megacity regions are summarized in Table 2.2.

² $\eta_1 \equiv 1$.

³ In this study, all trend estimators are given relative to the average value over the whole time period 1996–2010.

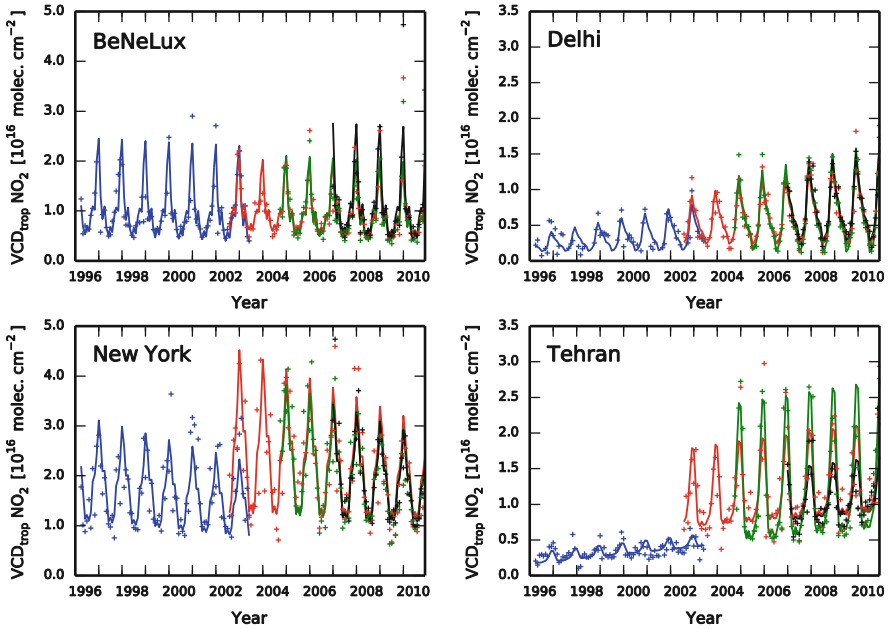


Fig. 2.1 Measured monthly averages $Y_{(t,i)}$ (crosses) and fitted trend function $X_{trend}(\hat{\theta}, t, i)$ (solid lines) for the four instruments GOME (blue), SCIAMACHY (red), OMI (green), and GOME-2 (black)

Table 2.2 Annual growth rates of linear ($\hat{\omega}$) and harmonic ($\hat{\xi}$) trend components for selected megacity regions for the 1996–2010 period, relative to the period’s average value

City	Linear trend ($\hat{\omega}$) (%/yr)	Harmonic trend ($\hat{\xi}$) (%/yr)
Athens	-2.6	-6.3
Baghdad	+9.2	+13.5
Barcelona	-2.3	-6.1
Beijing	+4.4	+5.9
BeNeLux	-2.2	-0.1
Cairo	+4.8	+13.0
Delhi	+5.0	+9.0
Hong Kong	+1.4	+1.1
New York City	-4.2	-5.6
Po Valley	-2.3	-1.5
Tehran	+4.4	+1.3
Tokyo	-3.5	-4.9

2.1.4 Discussion and Conclusion

The observed decreases in tropospheric NO₂ abundances throughout the developed world follow the improvements which have been made in reducing emissions and

fighting air pollution. For example, NO_x emissions in Europe have reportedly dropped by 30 % from 1990 to 2000 and by 18 % from 1996 to 2002 (Lövblad et al. 2004). In the developing world, the increases in $\text{VCD}_{\text{trop}} \text{NO}_2$ reflect the strong growth in energy consumption, which goes along with rapid economic growth. China, for example, has seen a 64 % increase in NO_x emissions from 1996 to 2004 (Zhang et al. 2007).

The derived trend estimators show generally good agreement with previous trend studies (van der A et al. 2008; Konovalov et al. 2010). Perfect agreement however cannot be expected, because trend analyses of relatively short time series depend very strongly on the exact period covered and the used methodology.

While NO_2 shows a pronounced diurnal cycle,⁴ the small timespan of e.g. 30 min between GOME and SCIAMACHY measurements cannot be the only reason for the observed differences between the four instruments. Model inter-comparison studies suggest that NO_2 levels at the instruments' overpass times differ by at most 10 % (Huijnen et al. 2010).

The spatial resolution of the satellite measurements however has significant effect on the observed NO_2 levels. The larger the pixel size, the more inhomogeneous are the actual NO_2 levels in the troposphere within the area covered by one measurement, and the more the high pollution peaks of e.g. megacities are smeared out by the spatial integration of the instrument. Using topography (U.S. Geological Survey 2004) and population density (Center for International Earth Science Information Network et al. 2005) data, this can be seen very clearly using the example of the three cities Delhi, New York, and Tehran. In Delhi, which lies in a topographically flat region with homogeneously high population density, virtually no difference between the four instruments can be observed. Under these conditions, emitted NO_2 can spread without barriers. The area around New York City is also topographically flat, but the densely populated area (as a proxy for areas with high NO_x emissions) is restrained to the landmass, which makes up only 2/3 of the whole area. Therefore, emitted NO_2 can spread towards the ocean, leading to NO_2 column gradients within the observed area. This NO_2 gradient between megacity and open ocean leads to the noticeable impact of the instrument's pixel size on retrieved VCD_{trop} . In the case of Tehran, emissions are restrained to the city's boundaries, as it lies in a desert region. Moreover, the emitted NO_2 cannot spread evenly throughout the area, because Tehran is bordered by the Alborz mountain range towards the North and East, leading to inhomogeneous NO_2 pollution in the observed area and thus to lower NO_2 columns in case of large pixel sizes.

We conclude that satellite observations are very well suited to observe tropospheric NO_2 pollution over megacities: decreasing and increasing trends can be observed in developed and developing countries, respectively. In spite of principally identical measurement conditions all over the globe, special attention must be paid to the spatial resolution of the instrument and to the spatial patterns of

⁴ In urban areas, the diurnal cycle of NO_2 is dominated by rush hour traffic peaks.

emissions and topography, as the selection of the measurement area, combined with differing spatial resolution of the available satellite instruments, strongly impacts the retrieved NO₂ values.

2.2 A Brief Example on the Application of Remotely Sensed Tracer Observations in Atmospheric Science—Studying the Impact of Stratosphere–Mesosphere Coupling on Polar Ozone Variability

Christoph G. Hoffmann¹ (✉), Matthias Palm¹, Justus Notholt¹,
Uwe Raffalski² and Gerd Hochschild³

¹Institute of Environmental Physics, University of Bremen, Germany

e-mail: christoff.hoffmann@iup.physics.uni-bremen.de

²Swedish Institute of Space Physics Kiruna, Sweden

³Institute for Meteorology and Climate Research, Karlsruhe Institute of Technology, Germany

Abstract This section outlines the realization and application of tracer observations in atmospheric science using an example in the context of ozone research; one particular factor contributing to polar ozone variability, namely the descent of mesospheric air into the stratosphere, is quantified. The estimation of this quantity, with results in a velocity of roughly 300 m/d, is outlined on the basis of ground-based microwave radiometry measurements of carbon monoxide in the Arctic.

Keywords Mesosphere–stratosphere coupling · Tracer observation · Ozone variability · Remote sensing · Microwave radiometry · Energetic particle precipitation · Atmospheric carbon monoxide

2.2.1 Introduction

The stratospheric ozone layer is one of the atmospheric key components of the climate system. It does not only absorb harmful ultraviolet (UV) radiation, but it also plays a major role for stratospheric temperatures and has indirect effects on the atmospheric circulation. The focus of ozone related research has been shifting from the understanding of the Antarctic ozone hole and Arctic ozone depletion towards the interaction of the (recovering) ozone layer and climate change in the last decade, demonstrating the importance of couplings between the individual layers of the atmosphere and other components of the climate system. On the one hand, climate change is expected to affect the ozone recovery (WMO 2007). On the other hand, the perturbed ozone layer influences the current climate, which

has to be considered in climate change research. E.g., the global trend of increasing mean surface temperatures seems to be masked in the inner of the Antarctic continent by ozone hole related effects (Thompson and Solomon 2002).

To understand these interactions more accurately, it is necessary to understand both, the natural and the human-induced ozone variability in more detail. The refined knowledge is finally used to improve the performance of current climate models, which become more realistic by including more climate components and their mutual couplings.

Natural polar ozone variability is partly caused by the dynamical variability of the polar winter atmosphere, which affects ozone directly through transport or indirectly through changes of temperature and chemistry. The general aim of this study is the observation of the dynamical evolution of the polar winter stratosphere and mesosphere from the ground. This is conducted indirectly by measuring carbon monoxide (CO), which acts as tracer for dynamics in this region, using microwave remote sensing.

One of the processes particularly studied with this approach, is the energetic particle precipitation (EPP) indirect effect (Randall et al. 2009). It refers to the penetration of high energetic particles from the sun or from space into the mesosphere and lower thermosphere (MLT) region (at about 100 km altitude). There, they interact with atmospheric constituents and form NO_x among others. The meridional circulation in the mesosphere is directed towards the winter pole and leads to a descent of air above the winter pole, so that this NO_x can be transported into the polar winter stratosphere, where it contributes as catalyst to ozone depletion. The strength of the descent determines how much NO_x enters the stratosphere, and also how deep it descends, i.e., if it will reach the ozone layer. It is therefore shown in this study, how the strength of the descent can be estimated from CO observations.

2.2.2 CO as Tracer in the Polar Stratosphere and Mesosphere

CO is largely produced in the MLT region by the photolysis of CO_2 . In the stratosphere and lower mesosphere, however, a loss reaction involving OH is dominant. The volume mixing ratio (vmr) profile of CO exhibits therefore a steep increase with altitude between both regions (Fig. 2.2). Furthermore, these chemical reactions are inactive in the absence of sunlight. Therefore CO has a long chemical lifetime particularly during polar night, so that changes of the vmr profile in these conditions must be due to dynamics. Thus, CO can there be used as tracer for dynamical processes (Solomon et al. 1985) and particularly for the descent of air above the winter pole, since the high CO values are shifted to lower altitudes by the winter descent (Fig. 2.2). In turn, from a time series of CO profiles, the properties of the vertical motion can be examined.

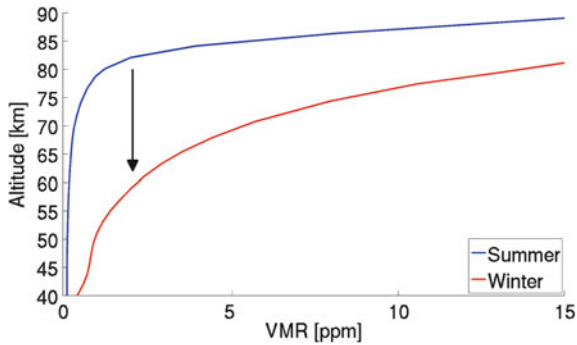


Fig. 2.2 Sketch of CO profiles during summer and winter demonstrating the downward shift of the higher CO vmr values as indicated with the *black arrow*

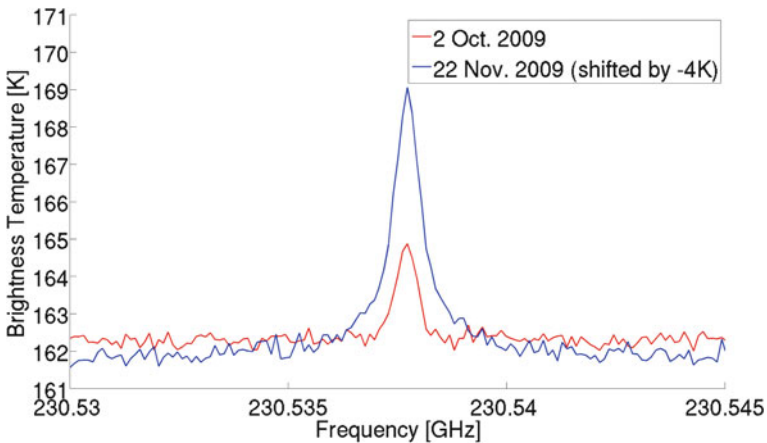


Fig. 2.3 Two examples of CO spectra. A relative change of the total CO abundance can be seen by eye (low CO abundance in *red* and high CO abundance in *blue*), whereas for the derivation of a CO profile a numerical process has to be performed, which separates the contributions from the single atmospheric layers

2.2.3 Measurements of CO by Microwave Radiometry

CO abundances of the stratosphere and mesosphere can be measured with several remote sensing techniques. Here we use ground-based microwave radiometry, which measures thermal emission of the atmosphere, thus can be used during polar night. Furthermore, this technique generally provides altitude-resolved information, so that vertical vmr profiles can be derived. The direct result of a single measurement is, however, not a vmr profile, but a microwave spectrum, showing the CO emission line at 230 GHz (Fig. 2.3). This line is a composite of the individual emissions of all atmospheric layers. The line shape of each individual emission is thereby dominantly controlled by the air pressure of the respective

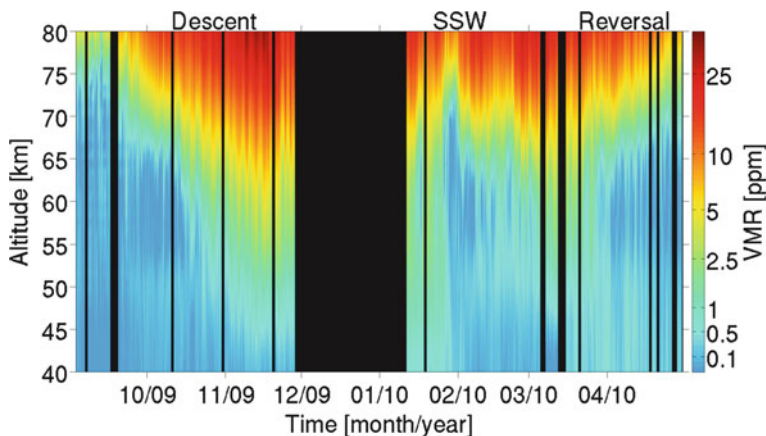


Fig. 2.4 Time series of KIMRA CO profiles showing all major features of dynamical variability throughout the winter 2009/2010

layer (pressure broadening), which is the key for the derivation of altitude-resolved data. The individual contributions to the composite have therefore to be deconvolved by a numerical process, the ‘retrieval’, to gain the vmr profile.

2.2.4 Interpretation of the KIMRA CO Time Series

The Kiruna Microwave Radiometer (KIMRA), used as example in this study, has been measuring microwave spectra of CO since 2007 in Kiruna, northern Sweden. The results of the retrieval of these spectra have recently been published (Hoffmann et al. 2011), showing that the measurement is sensitive between 40 and 80 km altitude. The corresponding time series of CO profiles for the winter 2009/2010 is shown in Fig. 2.4. The strong gradient of each CO profile is visible in the color-coding, and the descent of air during fall can be identified by the shift of similar colours from higher to lower altitudes. The average descent velocity can roughly be estimated by eye from the two altitudes of one particular CO level in October and in December, respectively, to be approx. 300 m/d (yellowish contours). This simple estimation works well for average velocities over a few months but is replaced by the analysis of the continuity equation of CO for more quantitative purposes.

Furthermore, the time series exhibits more CO variability starting at the end of January (Fig. 2.4), which corresponds to a dynamical perturbation known as sudden stratospheric warming (SSW). This strong dynamical perturbation is an important contribution to the variability of the polar winter stratosphere. Finally, the CO vmr decreases in spring, which is due to both, the reversal of the meridional circulation during the transit from winter to summer and the increasing exposure to sunlight in spring. All these dynamical features naturally influence the observed polar ozone variability, and are studied using such CO observations.

2.2.5 Summary and Conclusion

This section outlines the application of tracer observations in atmospheric science, showing how one particular factor can be quantified that finally contributes to the natural variability of the polar ozone layer. The initial interest is the strength of the descent of mesospheric air into the stratosphere and its representation in recent atmospheric models. Since the descent is not directly observable, a tracer for this motion, namely CO, is found based on its chemical properties. Since CO can also not be measured in situ, remote sensing is applied to measure spectra of the thermal emission of atmospheric CO from the ground. The CO vmr profiles are derived from these spectra, using a numerical retrieval technique.

The complete procedure has been outlined in this paper for the CO measurements of the radiometer KIMRA in the Arctic. The strength of the descent has been estimated to be roughly 300 m/d during the northern winter 2009/2010. A comparison of the presented CO time series with the Whole Atmosphere Community Climate Model (WACCM, Garcia et al. 2007) of the National Center for Atmospheric Research in Boulder, U.S.A. has been performed recently and has revealed a very good agreement (Hoffmann et al. 2012).

Acknowledgements The presented analysis of the CO data was supported by the German Research Foundation (Deutsche Forschungsgemeinschaft, DFG) with the projects NO 404/8-1 and PA 1714/3-2. The KIMRA instrument has initially been funded by the Knut and Alice Wallenberg Foundation. Substantial support for maintenance and development of the system was provided by the Swedish National Space Board and the Kempe Foundation.

2.3 Contamination of the Western Pacific Atmosphere

**Theo Ridder¹ (✉), Justus Notholt¹, Thorsten Warneke¹
and Lin Zhang²**

¹Institute of Environmental Physics, University of Bremen, Germany
e-mail: jnotholt@iup.physik.uni-bremen.de

²School of Engineering and Applied Sciences, Harvard University, Cambridge, MA, USA

Abstract The Western Pacific is one of Earth's most remote areas and air in this region belongs to the cleanest air worldwide. However, the global anthropogenic and natural release of trace gases causes increasing contamination of Western Pacific air masses. To improve the knowledge about Western Pacific air, pollution carbon monoxide and ozone distributions were measured in the Western Pacific during a ship campaign with research vessel *Sonne* in autumn 2009. Between Japan and New Zealand observations of atmospheric trace gases were performed using solar absorption Fourier Transform infrared spectrometry. Distinct plumes of

elevated carbon monoxide and ozone concentrations in the northern and southern hemisphere were observed. The cause of the measured air pollution is examined using a chemistry transport model showing that global scale transport of pollutants from Asia and Australia, but also partly from source regions as far away as Europe and Africa, causes the contamination of Western Pacific air. Generally, in the northern hemisphere a contamination of the Western Pacific air through fossil fuel combustion is dominant, while in the southern hemisphere trace gas emissions from biomass burning cause the most significant contamination.

Keywords Western Pacific · Remote sensing · Atmospheric modelling · Chemical composition · Carbon monoxide · Troposphere · Airmass transport · Air pollution

2.3.1 Introduction

The Western Pacific is one of the most remote areas on Earth. Due to the remoteness air in this region belongs to the cleanest air masses worldwide. However, the global increasing anthropogenic emission of trace gases (Solomon et al. 2007) and the emission of trace gases from natural sources cause contamination of the atmosphere in the Western Pacific. This contamination can occur by a direct release of trace gases in this region through e.g. ship and flight traffic (Eyring et al. 2005). An even more important factor is the global transport of air pollutants from continental source regions into the Western Pacific. These continental source regions include e.g. industrial urban centers in South–East Asia (Jacob et al. 2003) and biomass burning regions in Africa (Andreae and Merlet 2001).

The Earth's system reacts delicately to contamination of the Western Pacific atmosphere. The tropical Western Pacific is considered to be the main region where tropospheric air masses are transported into the stratosphere (Holton et al. 1995). This upwelling process is associated with transport of trace constituents from the troposphere into the stratosphere. An enhanced entry of tropospheric trace gases into the Western Pacific, thus, follows an enhanced entry of pollutants into the stratosphere. This entry of tropospheric pollutants can disturb the chemical equilibrium of the stratosphere and can have a strong impact on stratospheric chemistry. Recent investigations deal with problems, such as whether the current entry of tropospheric pollutants into the stratosphere causes a delay in stratospheric ozone recovery (WMO 2007).

Measurements of atmospheric trace constituents in the Western Pacific are rare. Thus, the composition of the Western Pacific atmosphere is not very well known. Furthermore, the impact of individual sources and source regions on Western Pacific air quality is not fully understood. Here, we investigate Western Pacific air contamination and analyze the origin of the pollution.

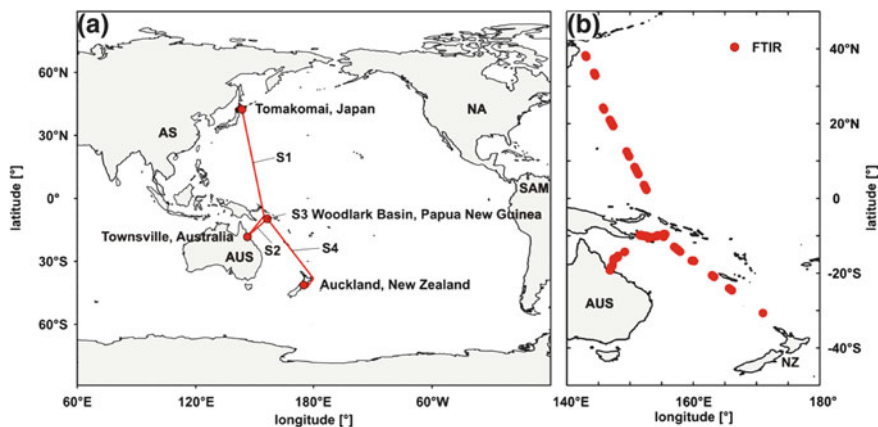


Fig. 2.5 **a** Overview of the ship campaign with RV *Sonne* in the Western Pacific divided into four cruise sections S1–S4. **b** Measuring points of the solar absorption FTIR spectrometer during the ship campaign

2.3.2 Method

To improve the knowledge about Western Pacific air contamination, atmospheric measurements of carbon monoxide (CO) and ozone (O₃) have been performed during a ship campaign with research vessel (RV) *Sonne* from Japan to New Zealand in autumn 2009. Aboard, solar absorption Fourier Transform infrared (FTIR) spectrometry (Rao and Weber 1992) was performed. The ship track is shown in Fig. 2.5. The measurements have been compared to a simulation with the full chemistry transport model *GEOS-Chem* for atmospheric composition (Bey et al. 2001) in order to evaluate the sources of the observed pollution.

2.3.3 Results

Figure 2.6 (top) shows the CO and O₃ distributions measured during the four sections of the ship campaign with RV *Sonne* (Fig. 2.5) in the Western Pacific. CO is presented as the total column amount, which describes the total amount of CO in the whole atmosphere above the observer. O₃ is pictured as the tropospheric column, which describes the total amount of O₃ in the troposphere above the observer. In comparison, the corresponding simulated CO and O₃ concentrations calculated with the *GEOS-Chem* model are presented showing that the simulations reproduce the observations well. Both distributions show several distinct plumes (PE1–PE3) of elevated CO and O₃ concentrations (PE1: beginning of cruise section S1, PE2: end of S1 and beginning of S2, and PE3: end of S3 beginning of S4).

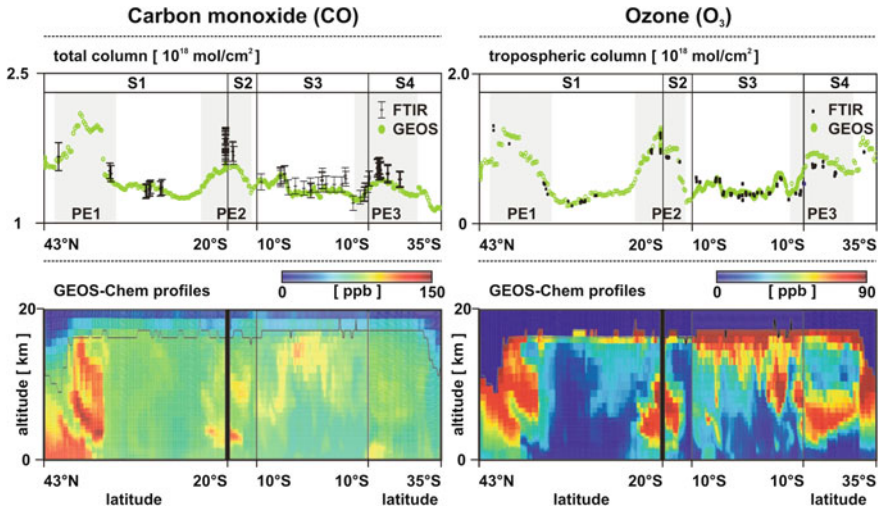


Fig. 2.6 CO and O₃ pollution in the Western Pacific measured during the ship campaign with RV *Sonne* and simulated with the *GEOS-Chem* model; *top* FTIR total and tropospheric column amounts compared to the *GEOS-Chem* model showing distinct plumes of elevated CO and O₃ (PE1–PE3), *bottom* *GEOS-Chem* vertical profiles showing the vertical distribution of the pollution

In order to get information about the vertical distribution of the contamination, the vertical profiles of CO and O₃ simulated with the *GEOS-Chem* model are shown in Fig. 2.6 (bottom). Pollution PE1 is distributed in the whole troposphere, pollution PE2 is apparent in the middle troposphere, and pollution PE3 occurs in the lower (CO) and middle (O₃) troposphere.

Within cruise section S3 elevated CO and O₃ in the upper troposphere is, furthermore, visible in Fig. 2.6 (bottom). Tropospheric air is vertically transported into the upper troposphere and can reach the stratosphere in this region. Thus, an example of the entry of tropospheric pollutants into the stratosphere is discovered.

2.3.4 Discussion and Conclusion

In order to determine the cause of the measured pollution in the Western Pacific, the *GEOS-Chem* model is used to calculate the contributions of various sources and source regions to the total pollution. Figure 2.7 shows the contribution of anthropogenic CO emissions from Asia and Europe (left) and contributions from biomass burning CO emissions (right) from Australia and Africa. Asian emissions are, according to this, the strongest CO source in the northern hemisphere with a direct impact on Western Pacific air quality. However, smaller European emissions are transported across Siberia towards the Western Pacific. North American anthropogenic emissions (not shown) only have a small impact on Western Pacific air composition.

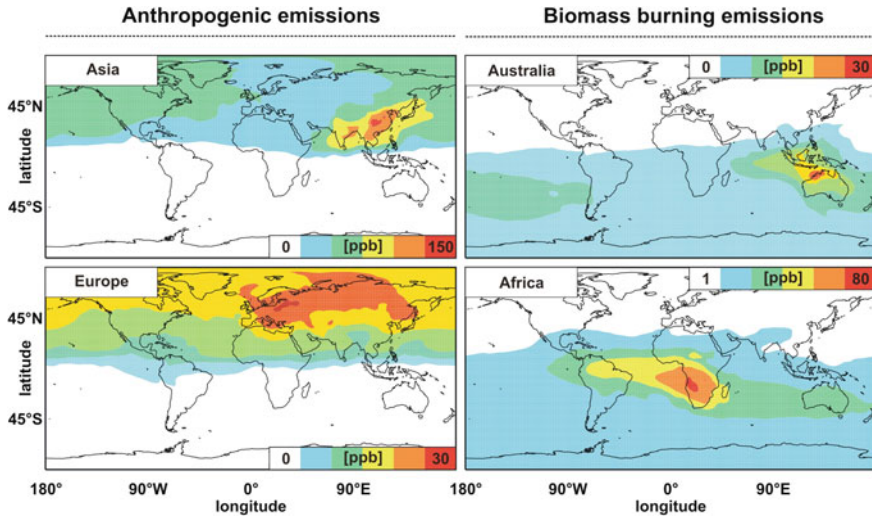


Fig. 2.7 Contributions from different sources and source regions to the measured pollution in the Western Pacific; *left* monthly mean (Oct. 2009) tropospheric average concentrations of anthropogenic CO emissions from Asia and Europe, *right* monthly mean (Oct. 2009) tropospheric average concentrations of biomass burning CO emissions from Australia and Africa

In the southern hemisphere the strongest source of CO pollution in the Western Pacific appears to be African biomass burning. Although most of African emissions are transported to the North-West, a significant plume of CO reaches the Western Pacific. In addition, biomass burning emissions in Australia considerably contribute to Western Pacific air contamination.

A detailed study about the contamination of the Western Pacific through CO and O₃ during the ship campaign with RV *Sonne* in autumn 2009 and an extensive evaluation of the sources and source regions of the measured pollution are published in Ridder et al. (2011).

2.4 Three Dimensional Model Simulations of the Impact of Solar Proton Events on Nitrogen Compounds and Ozone in the Middle Atmosphere

Nadine Wieters¹ (✉), Holger Winkler¹, Miriam Sinnhuber², Jan Maik Wissing³ and Justus Notholt¹

¹Institute of Environmental Physics (IUP), University of Bremen, Germany
e-mail: nwieters@iup.physics.uni-bremen.de

²Karlsruhe Institute of Technology, Germany

³Department of Physics, University of Osnabrück, Germany

Abstract Solar Proton Events (SPEs) can have a large impact on the composition of the upper and middle atmosphere. These events are caused by fluxes of high energetic protons emitted from the sun that enter the Earth's atmosphere mainly in polar regions. These particle fluxes lead to ionization in the mesosphere and stratosphere. This ionization produces nitrogen NO_x (N, NO, NO_2) and hydrogen HO_x (H, OH, HO_2) compounds that can destroy ozone (O_3) very effectively. We investigate the impact of SPEs on stratospheric chemistry, in particular on NO_x and O_3 , by means of model simulations with the Bremen 3-dimensional Chemistry and Transport Model (B3dCTM) for the period of the very large SPE in October/November 2003. Our simulations indicate a large increase of NO_x of about 200 ppb during the event. Since NO_x is rather long-lived during polar winter, modeled values for the Northern Hemisphere are continually enhanced by 20–100 ppb for several weeks after the event. These increased values are transported into the lower stratosphere within the polar vortex. During this downward transport, the enhanced NO_x values destroy up to 50 % of O_3 within the polar vortex, lasting until middle of December 2003. This O_3 depletion during the SPE 2003 can also be seen in observations.

Keywords Solar proton event · Energetic particle precipitation · Atmospheric modelling · Stratospheric chemistry · Ozone depletion · Polar vortex

2.4.1 Introduction

During Solar Proton Events (SPEs), huge solar eruptions, for instance, solar flares and Coronal Mass Ejections (CMEs), cause intense fluxes of protons with energies up to several hundred MeV. These particles can precipitate into the Earth's atmosphere along open magnetic field lines, therefore, mainly in polar regions. They can penetrate into different altitudes depending on their energies. Protons with energies of >1 MeV can enter the mesosphere, below 90 km, while protons with energies of >100 MeV can reach far into the stratosphere, below 40 km altitude. The precipitating particles lose their energy by collisions with high abundant atmospheric constituents such as nitrogen and oxygen, and produce ionization, dissociation, dissociative ionization, and excitation in the corresponding altitudes. The ionization and dissociation of N_2 leads to high amounts of NO_x (Porter et al. 1976; Rusch et al. 1981), whereas fast ion chemistry reactions produce high amounts of HO_x (Swider and Keneshea 1973; Solomon et al. 1981). These additional NO_x and HO_x compounds can destroy O_3 in catalytic reactions, whereby HO_x mainly destroys O_3 above 45 km and NO_x below 45 km (Lary 1997). Since energetic protons enter the atmosphere at both poles, these HO_x and NO_x productions occur in polar regions in both hemispheres. Because HO_x has a short lifetime (days), the impact on O_3 does not last very long, whereas the lifetime of NO_x constituents during polar night, in the absence of sunlight, is rather long

(weeks). The produced NO_x can then be transported downward within the polar vortex which forms during polar winter. This means, since the air in the vortex is isolated from neighbouring latitudes, O_3 depletion along the downward transport of the NO_x is nearly undisturbed, and therefore, reaches far into the lower stratosphere. This makes SPEs during polar winter interesting to investigate, since the O_3 depletion in lower altitudes derives from a combination of solar activity and atmospheric dynamics. The impact of SPEs on NO_x and O_3 have been studied in models (e.g. Jackman et al. 2005; Sinnhuber et al. 2003b; Wissing et al. 2010; Funke et al. 2011), and observations (see e.g. Seppälä et al. 2004; López-Puertas et al. 2005). In this study we use a Chemistry and Transport Model (CTM) which is driven by meteorological data to investigate the very large Solar Proton Event on October/November 2003 (hereafter referred to as ‘SPE 2003’).

2.4.2 Model Simulations

To study the impact of SPEs on mainly NO_x and O_3 , three-dimensional model studies have been performed with the B3dCTM. The model will be described briefly in the next section.

2.4.2.1 The B3dCTM

The Bremen 3-dimensional Chemistry and Transport Model (B3dCTM) has been developed as a combination of the chemistry transport model CTM-B (Sinnhuber et al. 2003a) with the chemistry code of the Bremen 2-dimensional model of the stratosphere and mesosphere (Sinnhuber et al. 2003b; Winkler et al. 2008). It computes the change in abundance of 58 species regarding chemical and dynamical forces. The dynamical forcing is prescribed by wind and temperature fields from, for instance, reanalysis of measurements, or modeled by general circulation models. The chemistry core computes about 180 neutral gas phase, photochemical, and heterogeneous reactions. The horizontal resolution is 3.75° in longitudinal and 2.5° in latitudinal direction. The vertical coordinate, in the model version used in this study, is potential temperature. This enables to calculate the vertical transport through diabatic heating and cooling rates. The vertical coverage is limited by the meteorological data set used. In this study, the ECMWF ERA-Interim (Dee et al. 2011) data set provided by the European Centre for Medium-Range Weather Forecasts (ECMWF) has been used. Hence, the vertical coverage of the model is 335–3231 K, about 10–60 km altitude.

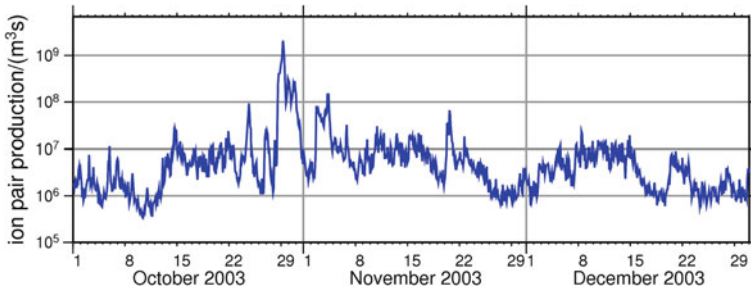


Fig. 2.8 AIMOS ionization rates due to proton precipitation averaged between 1 and 0.01 hPa over the Northern Hemisphere

2.4.2.2 Model Simulations of SPEs

To study the impact of SPEs, model simulations for the extremely large SPE on October/November 2003 have been performed. This SPE was one of the largest events in the past solar cycle. Huge CMEs have led to very high fluxes of energetic protons during October and November 2003, especially on 28/29 October and 3 November. To simulate the ionization impact of these particles, ionization rates derived from the Atmospheric Ionization Module Osnabrück (AIMOS) (Wissing and Kallenrode 2009) have been implemented into the B3dCTM. Figure 2.8 shows AIMOS ionization rates for this period averaged between 1 and 0.01 hPa over the Northern Hemisphere. The ionizing impact of the SPE is clearly seen in the mean ionization rates between 28 and 30 October 2003, and around the 4 November 2003, and is high during the whole period shown. Since the B3dCTM has a neutral chemistry core, the impact of the ionization needs to be parameterized. This was done by implementing production rates for NO_x and HO_x compounds based on Rusch et al. (1981), Porter et al. (1976) and Solomon et al. (1981). Accordingly, 1.25 NO_x (with 45 % N, and 55 % NO) and about 2 HO_x are produced per ion pair.

For this study, two model simulations have been performed. One model simulation assuming that no SPE occurred, hence no ionization rates included, and one with disturbed conditions, considering ionization rates based on precipitating protons.

2.4.3 Model Simulation Results

Figure 2.9 shows the impact of the SPE 2003 on HO_x (upper panel), NO_x (middle panel), and O_3 (lower panel). Each panel shows the difference of the two model runs described above. The values are differences of mean values within the band of 70–90° in high northern latitudes. The two upper panels of Fig. 2.9 show the direct impact of the ionization rates induced by the SPE as an increase of HO_x and NO_x ,

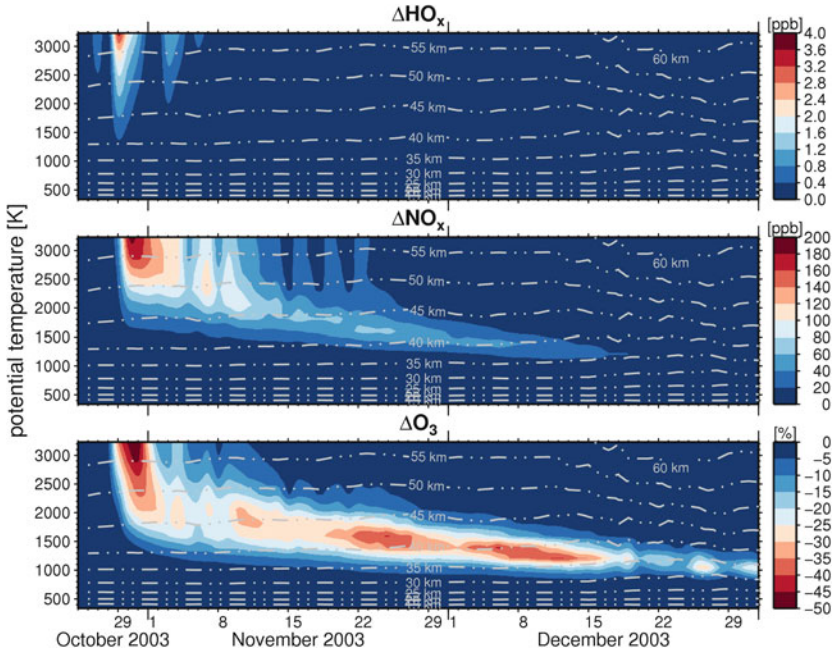


Fig. 2.9 Response in HO_x (*upper panel*), NO_x (*middle panel*), and O_3 (*lower panel*) to the SPE 2003 averaged over 70–90° North. See Sect. 3 for further details

largest at the days of highest ionization (see also Fig. 2.8). Increased HO_x values lead to O_3 depletion mainly above 45 km, which is also the main cause of the large modeled decrease of up to 50 % in O_3 during the first event around 30 October 2003. Since the SPE 2003 happened during northern polar winter, the directly produced NO_x was abundant for a long time, because of its long lifetime during polar night. During the event, the modeled NO_x is enhanced by about 200 ppb on 29/30 October 2003 and 100 ppb on 6 November 2003. Compared to background values assuming no SPE, this is an increase in NO_x by a factor of 500 and 200, respectively. A large fraction of the increased NO_x is then transported downwards within the polar vortex to lower altitudes, with enhancements of 40–80 ppb between 40 and 45 km lasting until the end of November 2003, and 20–60 ppb between 35 and 40 km lasting until middle of December 2003. The modeled NO_x enhancement between 35 and 45 km corresponds to an enhancement factor of 10–30, that leads to O_3 depletion of up to 40 %. Although the main O_3 depletion is diminished by the end of December, a small amount of NO_x values persists of up to several months after the event (not shown), leading then to an O_3 depletion of a few percent (see also Jackman et al. 2005).

2.4.4 Summary and Discussion

The impact of the SPE 2003 has been modeled with the B3dCTM. According to other model studies and observations (e.g. Seppälä et al. 2004; Jackman et al. 2005; López-Puertas et al. 2005; Wissing et al. 2010; Funke et al. 2011), the impact of this event is captured by the B3dCTM reasonably well. However, the impact on other species like HNO_3 (Verronen et al. 2008) and HCl (Winkler et al. 2009) are underestimated by a model that does not include any negative ion chemistry. This direct impact through negative ion chemistry needs to be parameterized additionally to the production rates described above. The influence of precipitating electrons on NO_x (Randall et al. 2007a, b; Sinnhuber et al. 2011) is not included here, but is currently under investigation. Model simulations (Wissing et al. 2010) indicate a direct impact of precipitating electrons on the ionization rates in the stratosphere, and therefore an impact on the production of NO_x in these altitudes. However, this issue is still not resolved since it has not been observed unambiguously yet (Funke et al. 2005; Clilverd et al. 2009; Funke et al. 2011). Model simulations, carried out with the B3dCTM with a similar setup, but including ionization rates due to proton and electron precipitation, seem to overestimate the production of NO_x (Funke et al. 2011).

Acknowledgments This work is financially supported by the Deutsche Forschungsgemeinschaft (DFG) within the priority programme CAWSES (Climate and Weather of the Sun–Earth System). The ECMWF ERA-Interim data have been obtained from the ECMWF Data Server.

2.5 Evaluation of the Coupled and Extended SCIATRAN Version Including Radiation Processes Within the Water: Initial Results

Mirjam Blum^{1,2} (✉), Vladimir Rozanov², Tilman Dinter^{1,2,3},
John P. Burrows¹ and Astrid Bracher^{1,2,3} (✉)

¹Institute of Environmental Physics, University of Bremen, Germany
e-mail: astrid.bracher@awi.de

²Helmholtz University Young Investigators Group PHYTOOPTICS

³Alfred Wegener Institute for Polar and Marine Research, Bremerhaven, Germany
e-mail: astrid.bracher@awi.de

To date, the software package SCIATRAN (Rozanov et al. 2002, 2005, 2008) has been used for modelling radiative processes in the atmosphere for the retrieval of trace gases from satellite data from the satellite sensor SCIAMACHY (Scanning Imaging Absorption Spectrometer for Atmospheric CHartography onboard the satellite ENVISAT). This SCIATRAN version only accounted for radiative transfer within the atmosphere and reflection of light at the earth surface. However,

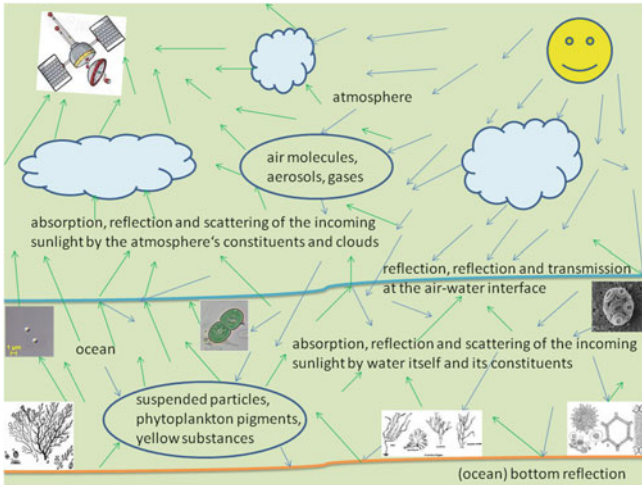


Fig. 2.10 Scheme of atmospheric and oceanic coupled radiative transfer

radiation also passes the air–water interface, proceeds within the water and is modified by the water itself and the water constituents. Therefore, SCIATRAN has been extended by oceanic radiative transfer and coupling it to the atmospheric radiative transfer model under the terms of established models for radiative transfer underwater (Kopelevich 1983; Morel et al. 1974, 2001; Shifrin 1988; Buitevald et al. 1994; Cox and Munk 1954a, b; Breon and Henriot 2006; Mobley 1994) and extending the data bases to include the specific properties of the water constituents (Pope and Fry 1994; Haltrin 2006; Prieur and Sathyendranath 1981) (Fig. 2.10).

So far, the coupling for the scalar radiative transfer is included. To analyse the quality of this new scalar coupled ocean–atmosphere radiative transfer version of SCIATRAN, model results of this and of the uncoupled SCIATRAN version are compared to satellite observations. In particular, we compared top of the atmosphere reflectances of the satellite sensor MERIS with the same parameters calculated with SCIATRAN by simulating the same optical conditions as for the satellite measurements. The MERIS data were selected in order to have different chl-a concentrations at different sites during different seasons. The main input parameters required for both SCIATRAN versions to simulate the selected MERIS collocations were concentrations of water vapour, ozone, chlorophyll, aerosol optical thickness, observation and illumination geometry, which were taken from the MERIS satellite and AERONET data sets. Both SCIATRAN versions consider the optical properties of organic and inorganic small (phytoplankton, bacteria, dust etc. $<1 \mu\text{m}$) and large (phytoplankton, zooplankton, sand etc. $\geq 1 \mu\text{m}$) particles. Furthermore, in the coupled SCIATRAN version the single scattering albedo and the extinction coefficient can be set. Both properties of water particles have an

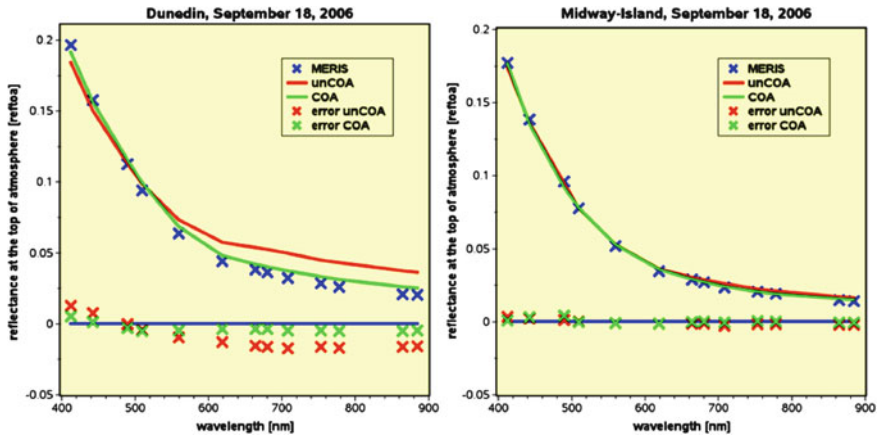


Fig. 2.11 Modelled (*red line* uncoupled, *green line* coupled SCIATRAN version) and measured (*blue cross* MERIS data) reflectances at the top of the atmosphere for (*left panel*) an oceanic region with chlorophyll concentration of 0.22 mg/m^3 , near the aerosol station Dunedin (New Zealand, 163.47° E and 42.59° S), and (*right panel*) an oceanic region with chlorophyll concentration of 0.09 mg/m^3 , near the aerosol station Midway Island (Atoll close to Hawaii, 177.35° W and 28.34° N), both on September 18, 2006. The *red crosses* show the deviation of the uncoupled version versus measured reflectance, and the *green crosses* the deviation of the coupled version versus measured reflectance in absolute values

important impact on the modelled result, but they are not often measured and not available from the MERIS satellite data at all. Therefore, common values based on theory and own tests have been used.

Figure 2.11 shows first results of these comparisons for two sites in the Pacific Ocean. Very good agreement (within 2–3 %) for both SCIATRAN versions was obtained with the satellite observation by MERIS measured close to Midway Island (Fig. 2.11 right). Deviations of the two SCIATRAN simulations are a bit larger (5–10 %) to the MERIS measurement close to the Dunedin station (Fig. 2.11 left). However, the deviations for both cases are at nearly all wavelengths smaller for the coupled SCIATRAN simulations, emphasizing the need to consider a coupled radiative transfer for retrievals of ocean color or atmospheric parameters over the ocean. Future studies will evaluate further the improved SCIATRAN version by focusing on MERIS collocations which overpass long-term-biooptical stations (e.g. BOSSOULE, MOBY) where more of the optical and geophysical parameters have been measured. Here the optical conditions under which MERIS observations were taken are clearer.

2.6 Improving the PhytoDOAS Method to Retrieve Cocolithophores Using Hyper-Spectral Satellite Data

Alireza Sadeghi¹ (✉), Tilman Dinter^{1,2,3}, Marco Vountas¹,
Bettina Taylor^{2,3} and Astrid Bracher^{1,2,3}

¹Institute of Environmental Physics, University of Bremen, Bremen, Germany
e-mail: sadeghi@iup.physics.uni-bremen.de

²Helmholtz University Young Investigators Group PHYTOOPTICS

³Alfred Wegener Institute for Polar and Marine Research, Bremerhaven, Germany

Abstract This study was dedicated to improve the PhytoDOAS method, which was established to distinguish major phytoplankton groups using hyper-spectral satellite data from SCIAMACHY. Instead of the usual approach of the PhytoDOAS single-target fit, a simultaneous fit of a certain set of phytoplankton functional types (PFTs) was implemented within a wider wavelength fit-window, called *multi-target fit*. The improved method was successfully tested through detecting reported blooms of coccolithophores, as well as by comparison of the globally retrieved coccolithophores with the global distribution of Particulate Inorganic Carbon (PIC). We analyzed eight years of SCIAMACHY data to investigate the temporal variations of coccolithophore blooms in a selected region within the North Atlantic, which is characterized by the frequent occurrence of intensive coccolithophore blooms. These data were compared to satellite total phytoplankton biomass, PIC concentration, sea-surface temperature, surface wind speed and modeled mixed-layer depth (MLD) in order to investigate the bloom dynamics based on variations in regional climate conditions. The results show that coccolithophore blooms follow the first total chlorophyll maximum and are in accordance with the PIC data. All three biological variables respond to the dynamics in wind speed, sea surface temperature and mixed layer depth. Overall, the results prove that PhytoDOAS is a valid method for retrieving coccolithophore biomass and for monitoring bloom developments in the global ocean.

Keywords Phyto-optics · SCIAMACHY · PhytoDOAS · Cocolithophores

2.6.1 Introduction

2.6.1.1 Motivation

The most suitable approach to monitor the global distribution of marine phytoplankton and to estimate their total biomass is by satellite remote sensing. Using ocean-color sensors, long-term records of aquatic parameters are provided on a global scale, with different applications (e.g., improving the understanding on

ocean biogeochemistry and marine ecosystem dynamics; assessing fisheries productivity and the distribution of harmful algal blooms). Surveying the distributions and developments of marine phytoplankton on a global scale (e.g. Yoder et al. 1993) has been done by retrieving aquatic chlorophyll-*a* (*chl-a*), the common phytoplankton pigment, which is used as an indicator of phytoplankton biomass (Falkowski 1998). Several biooptical empirical algorithms (e.g., OC4v4 by O'Reilly et al. 1998) and semi-analytical algorithms (Carder et al. 2004) have been developed, relying on water-leaving radiance detected by satellite sensors, to retrieve the total *chl-a*. However, due to the phytoplankton biodiversity and differences in the optical properties and biogeochemical impacts of different phytoplankton groups, remote identification of phytoplankton functional types (PFTs; Nair et al. 2008) has been of great interest. These developed PFT-based retrieval methods (e.g. Sathyendranath et al. 2004) will improve the estimates of the total phytoplankton biomass, as well as deepen the understanding of oceanic biogeochemical cycles. However, all these attempts have been dependent on empirical methods and therefore on a large sets of in situ measurements. This has motivated the development of an alternative method for retrieving PFTs, called PhytoDOAS (Bracher et al. 2009). This method is essentially different from the other PFT ocean-color algorithms by retrieving the optical signatures of different PFTs within the backscattered spectra measured by the hyper-spectral satellite sensor SCIAMACHY (on-board ENVISAT: ENVironmental SATellite of the European Space Agency, ESA). Testing the improvement of PhytoDOAS in retrieving more PFTs has been the main goal of this study.

2.6.1.2 The Importance of Coccolithophores

Sensitive responses of phytoplankton to environmental and ecosystem changes make them reliable indicators of the variations in climate factors. Coccolithophores are an abundant phytoplankton group with a wide range of impacts on the oceanic biogeochemical cycles and a significant influence on the optical features of surface water (Tyrrell et al. 1999). Coccolithophores emit dimethylsulfide (DMS, Andreae 1990), which is converted into the sulfur aerosols and cloud condensation nuclei (CCN), and thereby influence the climate and the Earth's energy budget (Charlson et al. 1987). Coccolithophore blooms are very important because they are frequently occurring (Holligan et al. 1993), and have unique biooptical and biogeochemical properties (Balch et al. 2004): coccolithophores are the main planktonic calcifiers in the ocean, characterized by building up calcium carbonate CaCO_3 plates, called *coccoliths* (Westbroek et al. 1985) and making a major contribution to the total content of suspended PIC in the open oceans (Milliman et al. 1993).

2.6.1.3 Objectives

The main interest of this study was to develop an appropriate method for quantitative remote sensing of coccolithophores using satellite data. This satellite-based method was used for monitoring temporal variations of coccolithophores on a global scale and by that for studying the impacts of variations of climate factors on marine phytoplankton. The study also aimed to identify the capacity and applicability of the method for climate research, i.e., phenological studies of phytoplankton dynamics to track the regional impacts of climate change (Winder 2010). In detail, coccolithophore dynamics in a selected region was monitored along with the variations of certain geophysical parameters, representing the regional climate. The retrieval method takes into account the phytoplankton absorption spectra, the existence of multiple PFTs and the pathlength of light penetrating in the water. These factors are often not considered in current biooptical methods based on band-ratio algorithms. Moreover, by retrieving only the differential absorption features, PhytoDOAS has the potential to obtain results on PFT *chl-a* also in coccolithophore rich region, where hyper-spectral variation are still visible. In this sense, retrieving coccolithophore blooms provides a reliable application to test the functionality of the improved PhytoDOAS method.

2.6.2 Material and Method

2.6.2.1 From DOAS to PhytoDOAS

PhytoDOAS was established to discriminate major phytoplankton groups based on their specific absorption footprints on the backscattered radiation from the ocean (Bracher et al. 2009). Differential Optical Absorption Spectroscopy (DOAS, Perner and Platt 1979), often used in atmospheric remote sensing, was applied to extract information on ocean optics; in particular on inelastic scattering (Vibrational Raman Scattering, VRS) of water molecules (Vountas et al. 2007) and on either diatoms or cyanobacteria specific absorptions. Within DOAS, from the ratio of earth shine backscattered radiation to extraterrestrial radiation, the imprints of differential absorption features of all relevant absorbers within the retrieved wavelength range are extracted. From the absorption cross-sections their differential parts are calculated by the *least square optimization*, which is used to fit the parameters attributed to the slant column densities of all relevant absorbers and the polynomial coefficients (accounting for elastic scattering and the low frequency variation in the absorption cross sections). The main outputs of PhytoDOAS are the fit factors for phytoplankton absorption and VRS, which are retrieved independently through two separate fits and are processed together to derive the *chl-a* concentration of the target PFT (Bracher et al. 2009).

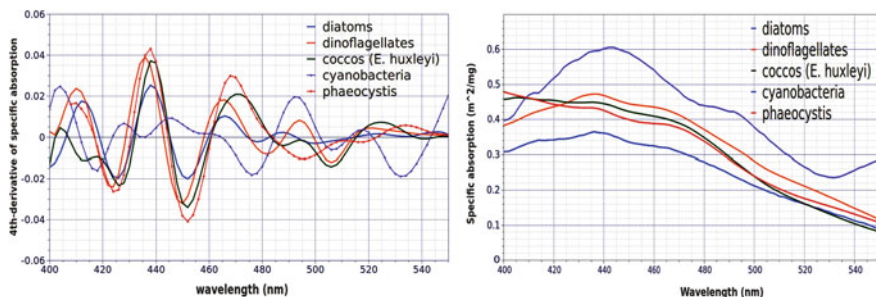


Fig. 2.12 Specific absorption spectra of five major PFTs (*right panel*) and corresponding fourth-derivative spectra (*left panel*) used for spectral analysis

2.6.2.2 Improvement to PhytoDOAS

As a recent improvement to PhytoDOAS, presented in this study, instead of just a single PFT target, three selected PFTs' absorption spectra (Fig. 2.12, left) are fitted simultaneously. These PFTs are diatoms, dinoflagellates and coccolithophores, which have been chosen through *derivative spectroscopy* analysis of phytoplankton absorption spectra (Aguirre et al. 2001). Based on the fourth derivative analysis, the appropriate PFTs (Fig. 2.12, right) for the simultaneous fit and also the appropriate fit-window for their retrieval (extended to 429–521 nm) have been selected. Accordingly, to incorporate the *multi-target fit* in PhytoDOAS, the single PFT absorption is replaced by several target PFTs' absorption spectra. The output includes a fit-factor assigned to each PFT target. The atmospheric reference spectra used in the PhytoDOAS *multi-target fit* are defined in (Bracher et al. 2009), the pseudo-absorption spectrum for VRS is defined in Vountas et al. (2007) and the target PFTs' spectra include the specific absorption spectra of diatoms, dinoflagellates and *E. huxleyi*, which were obtained by applying the PSICAM technique (Röttgers et al. 2007) on culture *E. huxleyi* and natural samples of diatoms and dinoflagellates. The *chl-a* conc. of PFTs existing in the natural samples were calculated by performing the CHEMTAX analysis (Mackey et al. 1996) on the high-performance liquid chromatography (HPLC) data.

2.6.2.3 Satellite and Modeled Data

For the PhytoDOAS method high spectrally resolved satellite data from SCIAMACHY have been used. This sensor covers a wide wavelength range (from 240 to 2380 nm) with a spectral resolution from 0.2 to 1.5 nm (Bovensmann et al. 1999). To compare and evaluate the PhytoDOAS coccolithophore results and to investigate their probable correlations with climate factors, four other satellite products were studied for a selected region in the North Atlantic from Jan. 2003 to Dec. 2010 as follows: (1) total *chl-a* from ESA's ocean-color dataset, GlobColour, providing

merged data from three major ocean-color sensors: MODIS-Aqua, MERIS and SeaWiFS, (<http://www.globcolour.info>); (2) PIC data from MODIS-Aqua level-3 products (<http://modis.gsfc.nasa.gov>); (3) sea surface temperature (SST) from Advanced Very High Resolution Radiometer sensor (AVHRR: <http://nsidc.org/data/avhrr>); and finally (4) surface wind-speed data derived from the Advanced Microwave Scanning Radiometer-Earth Observing System (AMSR-E) sensor (<http://remss.com>). Additionally, a set of mixed layer depth (MLD) modeled data, obtained from the Ocean Productivity's merged FNMOC data (<http://science.oregonstate.edu/ocean.productivity/index.php>), were used as another regional geophysical parameter. The PFT assimilated data from the NASA Ocean Biochemical Model (NOBM, (Gregg and Casey 2007)), were used as a preliminary source of comparison of PETs.

2.6.3 Results and Discussion

2.6.3.1 Global Distribution of Coccolithophores

Figure 2.13 illustrates, as an example, the global comparison of PhytoDOAS coccolithophore *chl-a* to PIC conc. for Aug. 2005, showing consistent patterns between the two products. Since the concentration of PIC is proportional to the suspended *coccoliths* in surface waters, it is regarded as an indicator for coccolithophores (Balch et al. 2005). In this sense, good agreements observed between the results of this study and PIC global distribution confirm the performance of the PhytoDOAS coccolithophore retrieval.

2.6.3.2 Time Series of Monitored Parameters in a Selected Region of the North Atlantic

To monitor the development of coccolithophore blooms, a region in the North Atlantic (named *nAtl*) at 53–63°N and 14–24°W of high bloom occurrence was selected based on the proposed global distribution of coccolithophores (e.g. Brown 1995) and on selected coccolithophore field studies (Holligan et al. 1993; Raitsos et al. 2006). Fig. 2.14 shows the monthly mean time series (from 2003 to 2010) of the PhytoDOAS coccolithophores and the other studied parameters: total *chl-a*, PIC, SST, wind-speed and modeled MLD. Table 2.3 shows the correlation coefficients over the bloom seasons in the *nAtl* region between the PhytoDOAS coccolithophores and the other parameters, and between PIC and other parameters.

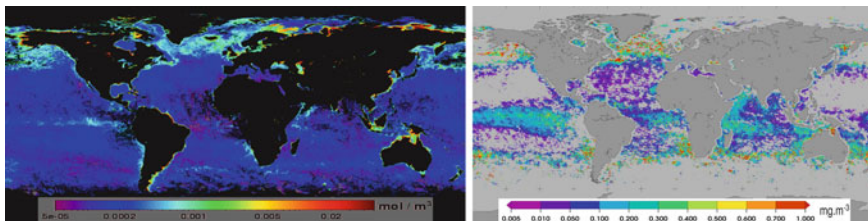


Fig. 2.13 PhytoDOAS coccolithophore *chl-a* from SCIAMACHY (right panel) and PIC conc. from the MODIS-Aqua (left panel) for Aug. 2005

2.6.4 Conclusions and Outlook

The PhytoDOAS results are consistent with the two other ocean color products, PIC conc. and total *chl-a*, and support the reported dependencies of coccolithophore biomass' dynamics to the compared geophysical variables. The results imply that coccolithophore blooms succeed the periods of elevated phytoplankton biomass, which are usually dominated by diatom blooms. Regarding the fact that the large reflectance from surface waters in coccolithophore rich areas affect the performance of the standard *chl-a* algorithms, the overestimations observed in the PhytoDOAS retrieved coccolithophores during the blooms (compared to the total *chl-a* product), suggest that over the coccolithophore bloom regions the ocean color sensors, supplying the GlobColour *chl-a* data, suffer from an underestimation of *chl-a*. However, the final assessment needs to be achieved by a future comprehensive validation with in situ measurements. This study suggests that PhytoDOAS is a valid method for retrieving coccolithophores' biomass and for monitoring bloom developments in the global ocean. Future applications of time-series studies using the PhytoDOAS data set are proposed, as using the new upcoming generations of hyper-spectral satellite sensors with improved spatial resolution. Regional adaptations of the PhytoDOAS coccolithophores are planned in order to account for the spatial variations in specific absorptions in respect to dominating coccolithophore species, e.g., following the well-known oceanic biogeophysical provinces (Longhurst 1998).

Acknowledgements We are thankful to ESA, DLR, and the SCIAMACHY Quality Working Group (SQWG) for providing us with SCIAMACHY level-1 data. We thank NASA-GSFC for NOBM data and MODIS PIC images and data. We are grateful to NASA and ESA, particularly to the GlobColour project, for supplying satellite total *chl-a* data. We are thankful to AVHRR for providing the SST data, AMSR-E for the surface wind-speed products and also Ocean Productivity for the monthly MLD data. Funding was provided by the HGF Innovative Network Funds (Phytooptics).

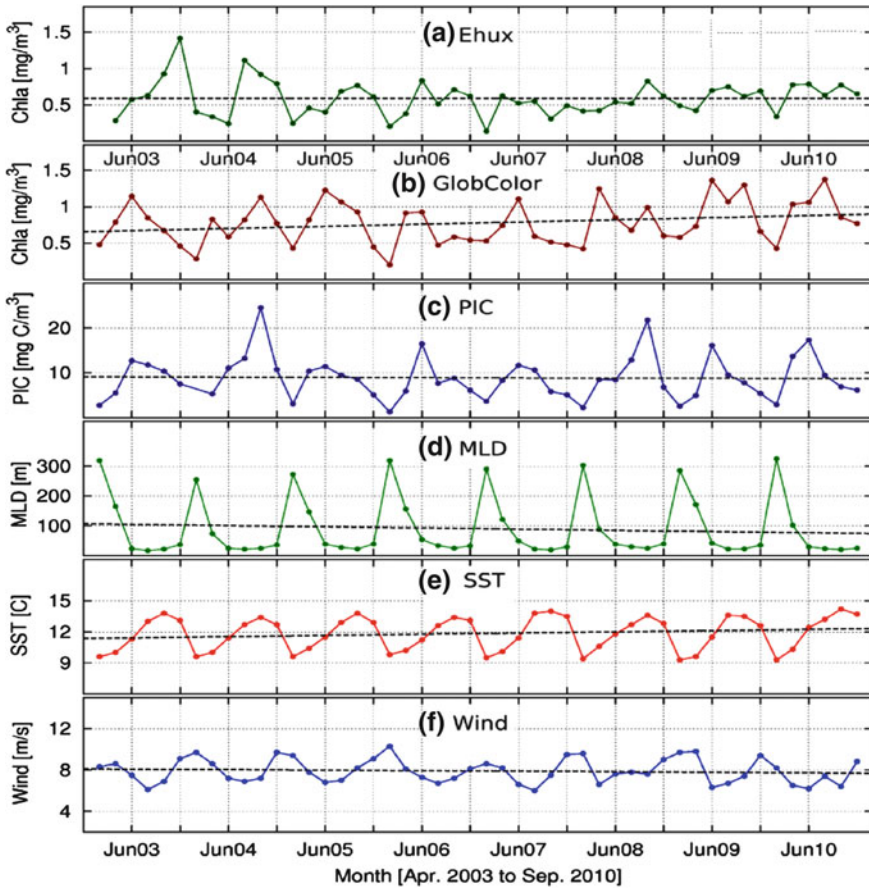


Fig. 2.14 Time series of six parameters monitored in North-Atlantic during the North Atlantic blooming season (January–September) from January 2003 to December 2010: **a** coccolithophores [Ehux] *chl-a* conc. retrieved by PhytoDOAS; **b** GlobColour total *chl-a*; **c** PIC conc. by MODIS-Aqua; **d** MLD from Ocean Productivity merged data; **e** SST from AVHRR; and **f** surface wind-speed from AMSR-E. The *dashed line* on each plot indicates the respective linear trend

Table 2.3 Correlation coefficients between the studied parameters in the North Atlantic region (*nAtl*)

	Ehux <i>chl-a</i> (PhytoDOAS)	Total <i>chl-a</i> (GlobColour)	PIC (MODIS -Aqua)	MLD	SST	Wind-speed
Ehux <i>chl-a</i>	–	0.53	0.66	–0.58	0.64	–0.49
PIC	0.66	0.79	–	–0.67	0.59	–0.72

2.7 Primary Productivity and Circulation Patterns Downstream of South Georgia: A Southern Ocean Example of the “Island Mass Effect”

Ines Borrione¹ (✉), Olivier Aumont² and Reiner Schlitzer¹

¹Alfred Wegener Institute for Polar and Marine Research, Bremerhaven, Germany
e-mail: ines.borrione@awi.de

²Laboratoire de Physique des Océans, Plouzané, France

Abstract Growth of phytoplankton in the Southern Ocean (SO) is largely limited by insufficient concentrations of the micronutrient iron, so that despite the large macronutrient reservoir, the SO is considered a High Nutrient Low Chlorophyll region. Therefore, phytoplankton growth is enhanced where exogenous iron is introduced to the system, for example downstream from islands. These confined regions sustain very rich ecosystems and are hot spots for atmospheric carbon dioxide drawdown. In this study, a combination of satellite derived measurements and model simulations are used to investigate the biological and physical environmental disturbances of the island of South Georgia (37°W, 54°S), which is located in the southwestern part of the Atlantic sector of the SO. We show not only that the island shelf is an important source of dissolved iron to the system, but also that the characteristic surface circulation patterns found downstream of the island play an important role in maintaining the shape and distribution of the developing phytoplankton bloom.

Keywords Southern Ocean · South Georgia · Island mass effect · Satellite observations · Primary productivity · High nutrient low chlorophyll regions · Biogeochemical modelling · Iron · ROMS · PISCES

2.7.1 Introduction

The Southern Ocean (SO, latitudes south of 40°S) covers 20 % of the global ocean, and surrounds the Antarctic Continent. The main hydrographic component is the Antarctic Circumpolar Current (ACC), an intense eastward flowing current encircling uninterrupted the continent.

The SO is a fundamental component of the Earth system and of its response to climate change (Marinov et al. 2006). Along portions of the Antarctic coast, the seasonal sea-ice formation generates intermediate and bottom waters which provide a major forcing to the global thermohaline overturning circulation, hence promoting heat, nutrient and gas fluxes with the other oceans.

Along the path of the ACC, upwelling of deeper waters replenishes surface waters with high concentrations of macronutrients (e.g., phosphates and nitrates) necessary for the growth of phytoplankton. However, due to insufficient concentrations of the trace metal iron, which is necessary for photosynthesis, algal growth in the SO is reduced, a reason why it is defined as a High Nutrient Low Chlorophyll (HNLC) region (Sarmiento and Gruber 2006).

Higher algal biomass is found where exogenous iron is introduced to the surface layers; among others, noteworthy sources are continental margins and atmospheric dust depositions (Tagliabue et al. 2009), as well as sea-ice melting (Lannuzel et al. 2007).

In situ investigations of the remote SO are generally limited to Austral summer, when most oceanographic cruises can be conducted. Consequently, satellite observations and modelling experiments are necessary tools to integrate with available in situ measurements. The former provide a quasi-synoptic view of regions as large as the SO, while the latter, albeit the necessary simplifications, allow for a virtual laboratory where to test hypothesis and better understand processes. Both tools were combined in the current study to investigate how and to what extent the sub-Antarctic Island of South Georgia generates an “Island Mass Effect”, in other words, influences the surrounding physical and biogeochemical environment.

South Georgia (SG) is a relatively small island of the southwest Atlantic sector of the SO, lying between two of the major ACC fronts: the Polar Front (PF) to the north, and the Southern ACC Front (SACCF) to the south. Amidst HNLC waters, downstream from the island develops an intense phytoplankton bloom, which is clearly detectable from satellite ocean color imagery (Fig. 2.15, refer also to (Park et al. 2010)) and in situ measurements (Korb and Whitehouse 2004). This highly productive system sustains a rich ecosystem and one of the largest commercial krill fisheries (Atkinson 2001); furthermore, due to the enhanced phytoplankton growth, which promotes the biological carbon pump, it is identified as one of the most important Antarctic regions of atmospheric carbon drawdown (Schlitzer 2002).

2.7.2 Data and Methods

Chlorophyll-a concentration (chl-a) estimates were derived from the satellite Sea-viewing Wide Field-of-View Sensor (SeaWiFS) at 9 km resolution. Due to the large number of data gaps caused by frequent cloud cover, only monthly composites were used. Ocean color images were retrieved between November and February (austral summer) and between 1997 and 2010.

Surface circulation patterns were estimated from the AVISO Satellite Absolute Dynamic Topography (ADT) measurements. Weekly products were retrieved, and averaged to form a monthly climatology corresponding to the same time period of the SeaWiFS observations.

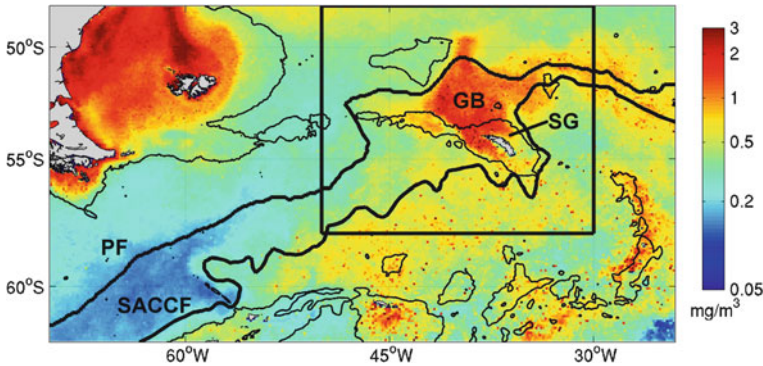


Fig. 2.15 November–February chlorophyll-a climatology from 1997 until 2010 in the southwest Atlantic sector of the SO from satellite ocean color estimates. *Bold lines* indicate the Polar Front (PF) and the Southern ACC Front (SACCF), *SG* indicates the island of South Georgia, and *GB* stands for Georgia Basin, the *rectangle* depicts the South Georgia region; *thin black lines* indicate the 2000 m isobaths

Model simulations were carried out with a coupled configuration of ROMS, a free surface, topography following, primitive equation regional model (Shchepetkin and McWilliams 2005) and PISCES, a 24-compartment biogeochemical model, where the cycles of carbon and the main nutrients (including iron) are resolved (Aumont and Bopp 2006). Simulations were run at $1/6^\circ$ resolution (~ 12 km).

2.7.3 Results and Discussion

According to the climatology shown in Fig. 2.15, a large phytoplankton bloom develops in the South Georgia region; the position of the bloom appears to be confined over the Georgia Basin while outside the basin borders, chl-a remains mostly below 0.5 mg/m^3 hence indicating typical HNLC conditions.

Measurements of ADT in the SG region, allow for estimating the main pathways and intensities of surface circulation; the former are parallel to ADT contour lines, while the latter are more intense when contour lines are closer. As indicated by ADT contours (black lines in Fig. 2.16a), the flow encounters the island from the southwest and then continues northeast embracing the Georgia Basin at all sides. Furthermore, it is possible to infer intense currents along the borders of the basin (especially along the northern periphery, where contour lines are closely spaced) and a weaker circulation regime in the region found directly above the basin.

The similarity between surface circulation patterns depicted in Fig. 2.16a and the bloom distribution shown in Fig. 2.15 suggests that the surface circulation in the SG region plays an important role in maintaining the shape and position of the

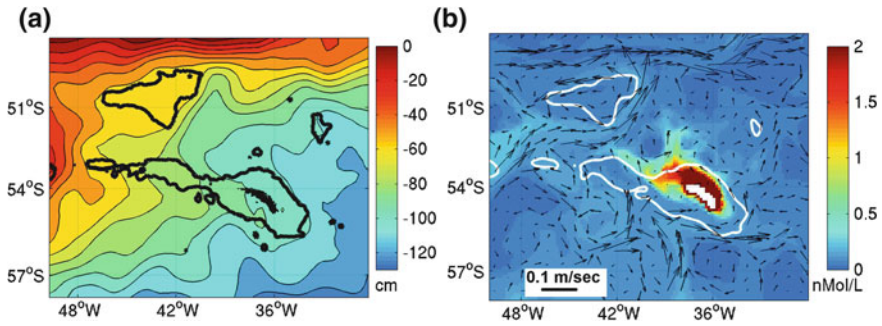


Fig. 2.16 **a** Absolute dynamic topography in the South Georgia region between November and February according to the 1997–2010 climatology. *Contour lines* indicate direction of main flow and distance between isolines provides an estimate of flow intensity. **b** Simulated distribution of surface dissolved iron (*color code*) and circulation (*arrows*) during December of model year 3. In both panels, 2000 m isobaths are indicated with *bold contour lines*

phytoplankton bloom developing downstream from SG. Therefore, circulation patterns are such that phytoplankton cells remain entrained in a favorable region where the flow is weaker and nutrient reservoirs may be continuously replenished.

The importance of SG as a source of dissolved iron is suggested by model simulations (Fig. 2.16b), which show the presence of a plume originating from the island that follows the direction of the main flow (arrows). However, the characteristic circulation patterns depicted in Fig. 2.16a remain difficult to resolve, possibly due to the sensitivity of the system to the adopted boundary conditions or the chosen model resolution which does not allow for a full representation of the physical environment (i.e., eddies, which at the chosen resolution are not resolved).

2.7.4 Conclusions

Although our results indicate that downstream from SG the observed phytoplankton bloom results from a characteristic physical environment, being SG a source of dissolved iron, a comprehensive understanding of the system, where a patchwork of top-down (i.e., grazing) or bottom-up (light or nutrient co-limitation) controls come into play, requires further in situ investigations and model experiments. The former would provide additional biogeochemical measurements which to date remain scarce, while the latter would help assess the relative importance of physical processes other than surface circulation (for example performing simulations where tidal effects and/or eddies are included) or additional nutrient sources in determining the observed biological response to the South Georgia “Island Mass Effect”.

2.8 Summer Sea Ice Concentration Changes in the Weddell Sea and Their Causes

Sandra Schwegmann¹ (✉), Ralph Timmermann¹, Rüdiger Gerdes^{1,2} and Peter Lemke^{1,3}

¹Alfred Wegener Institute for Polar and Marine Research, Germany

e-mail: sandra.schwegmann@awi.de

²Jacobs University, Bremen, Germany

³University of Bremen, Germany

Abstract Sea ice concentration, the fraction of sea ice coverage per unit area, is subject to regional climate variability in the Weddell Sea, Antarctica. The magnitude and origin of local trends in ice coverage, which are found to be most pronounced in summer, were analyzed using the “bootstrap algorithm sea ice concentration data” from the NSIDC for 1979–2006. The impact of atmospheric forcing such as air temperature and wind speed as well as that of ice drift obtained from satellite data and from free drift model simulations was studied. Generally, most of the observed sea ice concentration changes in summer can be related to wind changes. Also the temperatures correlate well with ice concentration, but whether sea ice concentration forced the temperature changes or vice versa is still unclear.

Keywords Sea ice · Concentration · Ice drift · Weddell Sea · Antarctic, Southern Ocean · SSM/I · Polar Pathfinder sea ice motion · Free drift · NCEP

2.8.1 Introduction

Sea ice is an indicator for climate change. In the Northern Hemisphere, ice extent (IE) has decreased over the last decades and the causes for this decrease have been subject to several studies (e.g. Parkinson and Cavalieri 2002; Stroeve et al. 2005). However, in the Southern Ocean, IE has increased by about 1 % per decade (Cavalieri and Parkinson 2008). This trend is a circumpolar average over different signals from various Antarctic regions. Here, we focus on the Weddell Sea sector.

Cavalieri and Parkinson (2008) found that the IE has increased during summer and fall by 6.3 and 1.8 %, respectively, and decreased during winter and spring by 0.1 %, but they were not able to fully identify the underlying mechanisms. We present an analysis of the sea ice concentrations (SIC) in the Weddell Sea for 1979–2006, showing that IE changes were a product of different trends in different parts of the Weddell Sea, namely (1) increasing SIC (and therefore a higher extent) in the eastern regions and (2) decreasing SIC along the Antarctic Peninsula. Our

analysis indicates that wind and related drift changes caused SIC trends and that their influences differ between the marginal and coastal ice zones and the pack ice in the central Weddell Sea.

2.8.2 Data

SIC data with a resolution of 25 km, projected onto a polar stereographic grid, are provided by the National Snow and Ice Data Center (NSIDC) as a combination of observations from the Scanning Multichannel Microwave Radiometer (SMMR) and the Special Sensor Microwave/Imager (SSM/I) generated using the bootstrap algorithm (Comiso 1999). Data were correlated to the NCEP/NCAR reanalysis sea level pressure, 2 m air temperature, and 10 m wind from 1979 to 2006 and to sea ice drift data from the Polar Pathfinder Sea Ice Motion vectors (Fowler 2003, obtained from the NSIDC), for 1988–2006. Uncertainties of this product for the Weddell Sea were quantified through a comparison with buoy data by Schwegmann et al. (2011) and have been shown to increase in summer. Therefore, we also used velocities from a free drift model, forced with 10-wind speeds and ocean near-surface currents from the Finite Element Sea ice-Ocean Model (FESOM, Timmermann et al. 2009).

2.8.3 Results and Discussion

Mean SIC (Fig. 2.17) and their trends (Fig. 2.18) were analysed in this study. The strongest changes of SIC occurred in austral summer, with an increase at the eastern boundaries of the ice cover and a strong decrease along the coast of the Antarctic Peninsula (AAP, Fig. 2.18). The changes at the AAP are observed year-round and can be related to increased wind speeds in most months. For all months, not only in summer, the wind velocities are anti-correlated with SIC in this region (Fig. 2.19). The zonal wind is thereby anti-correlated with SIC during all three months, whereas the correlation between the meridional component and SIC alternates in sign (not shown).

Generally, the same anti-correlation as for wind is found between observed SIC and modelled free drift next to the tip of the AAP (not shown). Mean sea ice drift at this location is offshore, transporting ice from the coast into the central Weddell Sea and the marginal sea ice zones. Thus, if sea ice drift is enhanced due to increased wind speeds, the near coastal region loses ice, while at the same time ice coverage is increased in the marginal sea ice zones. In the inflow area in the eastern Weddell Sea, free drift speeds are mainly anti-correlated to SIC. A feasible explanation is that with stronger drift, more sea ice can be transported into the Weddell Sea basin and less ice remains in the north-eastern coastal region, while refreezing only gradually increases the ice coverage in this region.

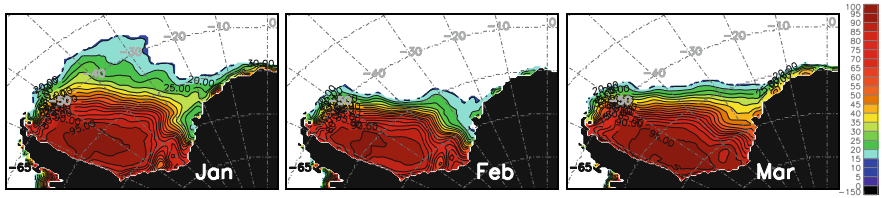


Fig. 2.17 Mean sea ice concentrations for January, February and March for the period 1979 through 2006 in %

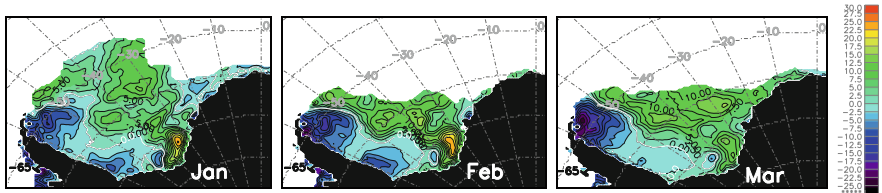


Fig. 2.18 Sea ice concentration trends in % concentration per decade

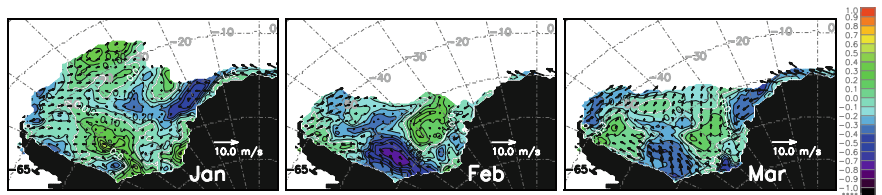


Fig. 2.19 Correlation between sea ice concentrations and wind speeds for January, February and March 1979–2006. *Vectors* show the mean wind field

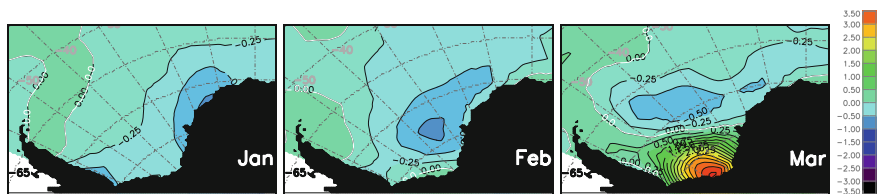


Fig. 2.20 Temperature trends for January, February and March 1979–2006

Next to the wind and the free drift, also temperatures show a significant signal: In February and March, 2 m air temperatures are mainly anti-correlated to SIC, with coefficients of up to -0.8 in the marginal sea ice zone (not shown). Specifically the decreasing SIC at the AAP comes along with increasing temperatures. Trends of the 2 m air temperatures (Fig. 2.20) at the AAP are indeed positive and are certainly connected to the observed decrease in SIC. In addition,

large parts of the Weddell Sea show a decrease in 2 m air temperatures in austral summer, which is consistent with increasing SIC in the marginal sea ice zone.

However, given that true observations in this region are sparse and that near-surface temperatures in the reanalysis datasets are bound to be affected by the SIC prescribed as a boundary condition in the assimilations system, it is impossible to tell whether warmer air forces ice to melt, or reduced ice coverage causes an increased ocean-to-air heat flux and thus a local warming of the lower atmosphere. An analysis of correlations with time lag of ± 1 month does not help to answer this question. In January, correlation of temperature changes one month behind those of SIC reveals a high anti-correlation (which indicates that reduced ice coverage causes a warming of the lower atmosphere), but for the other months, the highest anti-correlations occur without any time lag.

In addition, the analysis of cloud coverage does not yield a robust correlation to SIC, which may indicate that downward radiation fluxes do not play a major role in regional climate change in the Weddell Sea. Satellite-based ice drift patterns in summer are based on very few data points and show only little connection to the observed SIC changes.

2.8.4 Conclusion

Analyzed trends in near-surface wind and the closely connected ice drift are consistent with the observed decrease of SIC at the tip of the AAP together with the increased ice coverage in the eastern marginal sea ice zone. Correlation coefficients, however, are not very high, so that other effects certainly contribute to the observed changes. The finding that the correlations between simulated free drift and observed SIC are sometimes smaller than those for the reanalysis wind may result from the prescribed ocean currents as well as from the fixed mean sea ice thickness in the free drift model (although neither varying the prescribed mean sea ice thickness between 0.5 and 2 m nor using time-invariant ocean currents notably change the mean drift speeds), but it may also indicate that the advection of warm air with increased westerly winds adds to the purely dynamic effect. The weak connection between satellite-based ice drift and observed SIC may be due to uncertainties in the used satellite product, but further investigations on this topic are necessary.

2.9 Validation of the Snow Grain Size Retrieval SGSP Using Six Ground Truth Data Sets

Heidrun Wiebe¹ (✉), Georg Heygster¹ (✉) and Eleonora Zege²

¹Institute of Environmental Physics, University of Bremen, Germany
e-mail: heygster@uni-bremen.de

²B.I. Stepanov Institute of Physics of the National Academy of Sciences of Belarus
(IP- NASB)Minsk, Belarus

Abstract For climate modelling, the snow grain size is an important parameter to determine the snow albedo on ground, which in turn affects the radiative balance of the Earth. Recently, the Snow Grain Size and Pollution (SGSP) retrieval from reflectances of the optical satellite sensor Moderate Imaging Spectroradiometer (MODIS), applicable for polar regions, was developed and implemented. In this section, a comparison of the SGSP-retrieved with ground-measured snow grain size is presented, using six different ground truth data sets from the Arctic, the Antarctic, Greenland, and Japan. It shows a good agreement with a correlation coefficient of 0.86 and with small differences below 15 % for almost half of the comparison cases.

Keywords Snow grain size · Retrieval · MODIS · Validation

2.9.1 Introduction

Snow is part of the cryosphere in the climate system of the Earth. It covers up to 45.000 km² of the Earth's surface. As in most cases the snow falls on a darker surface, a much larger amount of the incoming solar radiation is reflected, affecting the radiative balance of the Earth.

From the microphysical perspective, a single snow grain is an ice crystal consisting of frozen water and is formed in clouds. The single crystals cluster together and fall as snow flakes onto the Earth's surface. There, they accumulate to a layer of snow consisting of ice, air, and sometimes impurities like dust or soot. Inside the snow layer, metamorphism changes the shape and size of the ice crystals, mainly controlled by the temperature and the vertical temperature gradient.

Light falling on a snow layer mostly gets scattered, reflected, and partly absorbed. As snow is a porous medium of ice, air, and possibly impurities, the light entering a snow layer is often multiply scattered. The albedo of snow (as the ratio of reflected (including multiply scattered) and incident light) is high in the visible (1.0–0.9) and decreases towards the near-infrared (0.9–0.2). For a semi-infinite snow layer, the albedo is mainly determined by the size and shape of the grains,

and the amount of impurities. Therefore, those parameters are important if modelling the Earth's climate.

Regular observations of the snow on a global scale can only be achieved by means of satellite remote sensing, as many snow covered areas in polar regions are difficult to access. The type of electromagnetic radiation sensitive to the snow grain size and impurities is the optical (visible and near-infrared) radiation in the range from 0.4 to 1.4 μm . Data in this spectral range are available from various satellite sensors at a spatial resolution in the order of 10 m–1 km.

An algorithm that uses optical observations to determine the snow grain size and impurity amount (here: soot concentration) with satellites is the Snow Grain Size and Pollution (SGSP) algorithm developed by Zege et al. (1998, 2008, 2011).

In this section, a validation study of the SGSP-retrieved grain size is summarized, using six ground truth data sets from different regions (Arctic, Antarctic, Greenland, and Japan) on different subsurfaces (land, sea ice, and lake ice) in the years 2001–2009. The full details are given in Wiebe et al. 2011.

2.9.2 The SGSP Retrieval

The SGSP algorithm, developed by Zege et al. (1998, 2008, 2011) computes the snow grain size and impurity amount from optical satellite data (here: MODIS Channels 3, 2, and 5 at 0.47, 0.86, and 1.24 μm). It uses a snow reflectance model based on an analytical asymptotic solution of the radiative transfer theory and on geometrical optics for the optical properties of snow (Zege et al. 2008):

$$R_i(\theta, \theta_0, \varphi) = R_0(\theta, \theta_0, \varphi) \exp\left(-A\sqrt{\gamma_i a_{ef}} \frac{K(\theta)K(\theta_0)}{R_0(\theta, \theta_0, \varphi)}\right) \quad (2.3)$$

with $\gamma_i = 4\pi(\chi_i + \kappa C_S)/\lambda_i$ and $K(\theta) = 3(1 + 2\cos\theta)/7$

- i refers to the MODIS Channel number i
- R_i is the snow reflectance received by the instrument
- R_0 is the bidirectional reflectance distribution function (BRDF) for non-absorbing snow
- θ , θ_0 , and φ are the sensor zenith, solar zenith, and relative azimuth angle
- A is a form factor depending on the snow crystal shape (here: $A = 5.8$)
- γ_i is the absorption coefficient of snow
- a_{ef} the effective optical snow grain size
- K is the escape function
- χ_i is the imaginary part of the complex refractive index of ice
- κ depends on the type of pollutant (here for soot: $\kappa = 0.2$)
- C_S is the relative volumetric soot concentration
- λ_i is the wavelength

Equation (2.3) is valid for retrievals directly on the surface, or for atmospherically corrected reflectances from satellite sensors. The atmospheric correction used in this work is described in Zege et al. (2011). Furthermore, two steps of data pre-processing are applied to the MODIS input data: removing striping artifacts due to instrument calibration errors and extracting snow pixels from non-snow pixels like water, soil, or clouds (Wiebe 2011).

The SGSP retrieval has two main characteristics distinguishing it from existing snow grain size retrievals (e.g. Nolin and Dozier 2000; Stamnes et al. 2007):

- Its reduced dependency on the snow crystal shape allows better results as the crystals may have different shapes (columns, plates, fractals) of different reflection characteristics, where the shape information is not available a priori on large areas in polar regions.
- Its validity at high solar zenith angles up to 75° (i.e. sun elevation down to 15°) allows applying the retrieval in polar regions where the sun is often low.

2.9.3 Validation Studies

The SGSP-retrieved snow grain size has been validated with ground truth data from six different measurements campaigns.

Aoki et al. (2007) measured the microphysical snow grain size by a handheld lens and ruler at several places on Hokkaido, Japan, and at Barrow, Alaska, in the years from 2001 to 2005. Gallet et al. (2010) measured the specific surface area (can directly be related to the optical snow grain size) at Dome C and on the traverse from Dome C to Dumont D'Urville, Antarctica, in the austral summer 2008/2009. Markus et al. (2006, Personal communication) measured the microphysical snow grain size on the sea ice of the Chuckchi Sea, Alaska. Scambos et al. (2007) measured the optical snow grain size by a ground spectrometer on the sea ice near the coast of Wilkesland, Antarctica. Painter et al. (2007) measured the optical snow grain size by a ground spectrometer at Swiss Camp near the west coast of Greenland. Brandt et al. (2008) measured the spectral albedo (can directly be related to the optical snow grain size) by a ground spectrometer, on the Elson Lagoon, Alaska.

The results of the six comparisons are shown in the scatter plot of Fig. 2.21, having a correlation coefficient $R = 0.86$. There are 17 cases with small differences below 15 %, 15 cases with intermediate differences between 15 and 50 %, and 5 cases with large differences above 50 %.

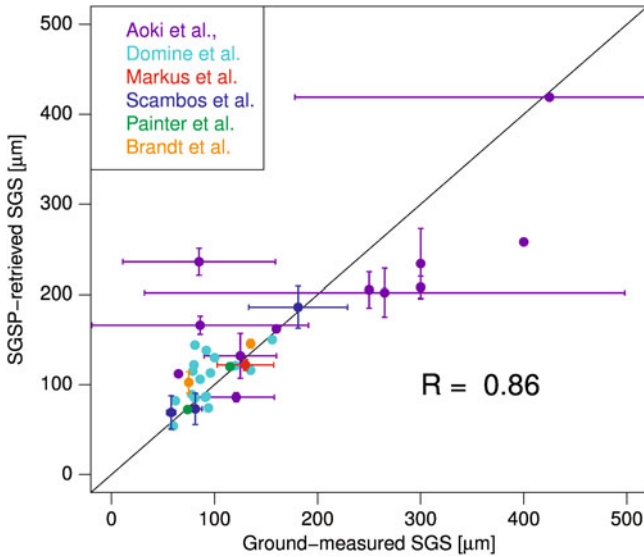


Fig. 2.21 Scatter plot of the SGSP-retrieved versus the ground-measured snow grain size for the 6 different data sets. *Dots* and *error bars* are local daily averages and their standard deviation. For cases without error bars only one measurement was available or the error was too little

2.9.4 Discussion and Conclusion

The comparison of the SGSP-retrieved to the ground-measured snow grain size from the six ground truth data sets shows a good agreement. Most cases of larger differences are influenced by cirrus clouds, wet snow, surface hoar, or wind crust. Discrepancies may also be attributed to SGSP retrieval, e.g. by instrument noise in the MODIS input data. Furthermore, the ground measurements are point measurements, whereas one satellite pixel has a size of $500 \times 500 \text{ m}^2$ inside of which the snow may not be distributed homogeneously.

In the Aoki et al. (2007) data set, measuring the microphysical snow grain size, the ground observations have a large spread at one site and day (large error bars in Fig. 2.21) and larger discrepancies to the SGSP-retrieved grain size. Therefore, ground measurements of the optical snow grain size are preferable for validating satellite retrievals.

The final result of this work is that the SGSP retrieval has been validated successfully with a versatile mixture of ground measurements. It is implemented in a near-real time processing chain allowing efficient processing of the snow grain size, which influences the albedo and thus the radiative balance of the Earth.

References

- Aguirre-Gomez R, Weeks AR, Boxall SR (2001) The identification of phytoplankton pigments from absorption spectra. *Int J Remote Sens* 22(2):315–338
- Andreae MO (1990) Ocean–atmosphere interactions in the global biogeochemical sulfur cycle. *Marine Chem* 30:1–29
- Andreae MO, Merlet P (2001) Emission of trace gases and aerosols from biomass burning. *Global Biogeochem Cycles* 15:955–966
- Aoki T, Hori M, Motoyoshi H, Tanikawa T, Hachikubo A, Sugiura K, Yasunari T, Storvold R, Eide H, Stannes K, Li W, Nieke J, Nakajima Y, Takahashi F (2007) ADEOS-II/GLI snow/ice products—part II: validation results using GLI and MODIS data. *Remote Sens Environ* 111:274–290. doi:[10.1016/j.rse.2007.02.035](https://doi.org/10.1016/j.rse.2007.02.035)
- Atkinson A, Whitehouse MJ, Priddle J, Cripps GC, Ward P, Brandon MA (2001) South Georgia, Antarctica: a productive, cold water, pelagic ecosystem. *Mar Ecol Prog Ser* 216. doi:[10.3354/meps216279](https://doi.org/10.3354/meps216279)
- Aumont O, Bopp L (2006) Globalizing results from ocean in situ iron fertilization studies. *Glob Biogeochem Cycles* 20. doi:[10.1029/2005GB002591](https://doi.org/10.1029/2005GB002591)
- Balch WM (2004) Re-evaluation of the physiological ecology of coccolithophores. In: Thierstein HR, Young JR (eds) *Coccolithophores. From molecular processes to global impact*. Springer, Berlin, pp 165–190
- Balch WM, Gordon HR, Bowler BC, Drapeau DT, Booth ES (2005) Calcium carbonate measurements in the surface global ocean based on moderate-resolution imaging spectroradiometer data. *J Geophys Res* 110:C07001
- Bey I, Jacob DJ, Yantosca RM, Logan JA, Field BD, Fiore AM, Li Q, Liu HY, Mickley LJ, Schultz MG (2001) Global modeling of tropospheric chemistry with assimilated meteorology: Model description and evaluation. *J Geophys Res* 106:23073–23095
- Bovensmann H, Burrows JP, Buchwitz M, Frerick F, Noël S, Rozanov VV (1999) SCIAMACHY: mission objectives and measurement modes. *J Atm Sci* 56:127–150
- Bracher A, Vountas M, Dinter T, Burrows JP, Röttgers R, Peeken I (2009) Quantitative observation of cyanobacteria and diatoms from space using PhytoDOAS on SCIAMACHY data. *Biogeosciences* 6:751–764
- Brandt R, Gerland S, Pedersen C, Berntsen T, Borgar A (2008) Spectral albedo of the snow surface: Elson Lagoon, Barrow, AK. http://www.atmos.washington.edu/sootinsnow/PDF_Documents/Brandt_et_al_2005.pdf. Accessed 18 Oct 2010
- Breon FM, Henriot N (2006) Spaceborne observations of sun glint reflectance and modeling of wave slope distributions. *J Geophys Res* 111:C06005. doi:[10.129/2005JC003343](https://doi.org/10.129/2005JC003343)
- Brown CW (1995) Global distribution of coccolithophore blooms. *Oceanography* 8(2):59–60
- Buitevald H, Hakvoort JHM, Donze M (1994) The optical properties of pure water. *SPIE Ocean Optics XII* 2258:174–183
- Burrows JP, Weber M, Buchwitz M, Rozanov VV, Ladstaetter-Weissenmayer A, Richter A, DeBeek R, Hoogen R, Bramstedt K, Eichmann K-U, Eisinger M (1999) The global ozone monitoring experiment (GOME): mission concept and first scientific results. *J Atm Sci* 56:151–175
- Callies J, Corpaccioli E, Eisinger M, Hahne A, Lefebvre A (2000) GOME-2—Metop’s second-generation sensor for operational ozone monitoring. *ESA Bulletin* 102:28–36
- Carder KL, Chen FR, Cannizzaro JW, Campbell JW, Mitchell BG (2004) Performance of the MODIS semi-analytical ocean color algorithm for chlorophyll-a. *Adv Space Res* 33:1152–1159
- Cavaliere DJ, Parkinson CL (2008) Antarctic sea ice variability and trends, 1979–2006. *J Geophys Res (Oceans)* 113:C07004. doi:[10.1029/2007JC004564](https://doi.org/10.1029/2007JC004564)
- Center for International Earth Science Information Network (CIESIN) (2005) Columbia University, United Nations Food and Agriculture Programme (FAO), and Centro Internacional de Agricultura Tropical (CIAT). *Gridded Population of the World: Future Estimates*

- (GPWFE). Palisades, NY: Socioeconomic Data and Applications Center (SEDAC). Columbia University
- Charlson RJ, Lovelock JE, Andreae MO, Warren SG (1987) Oceanic phytoplankton, atmospheric sulfur, cloud albedo and climate. *Nature* 326:655–661
- Clilverd MA, Seppälä A, Rodger CJ, Mlynarczyk MG, Kozyra JU (2009) Additional stratospheric NO_x production by relativistic electron precipitation during the 2004 spring NO_x descent event. *J Geophys Res* 114:A04305
- Comiso J (1999) Bootstrap sea ice concentrations from Nimbus-7 SMMR and DMSP SSM/I, 1979–2007. National Snow and Ice Data Center, Boulder. Digital media (1999, updated 2008)
- Cox C, Munk W (1954a) Statistics of the sea surface derived from sun glitter. *J Mar Res* 13(N2):198–227
- Cox C, Munk W (1954b) Measurement of the roughness of the sea surface from photographs of the Sun's glitter. *J Opt Soc Am* 44(11):838–850
- Dee DP, Uppala SM, Simmons AJ, Berrisford P, Poli P, Kobayashi S, Andrae U, Balmaseda MA, Balsamo G, Bauer P, Bechtold P, Beljaars ACM, van de Berg L, Bidlot J, Bormann N, Delsol C, Dragani R, Fuentes M, Geer AJ, Haimberger L, Healy SB, Hersbach H, Hólm EV, Isaksen L, Kållberg P, Köhler M, Matricardi M, McNally AP, Monge-Sanz BM, Morcrette J–J, Park B–K, Peubey C, de Rosnay P, Tavolato C, Thépaut J–N, Vitart F (2011) The ERA-interim reanalysis: configuration and performance of the data assimilation system. *Quart J R Met Soc* 137:553–597
- Eyring V, Köhler HW, van Aardenne J, Lauer A (2005) Emissions from international shipping: 1. The last 50 years. *J Geophys Res* 110:D17305
- Falkowski PG, Barber RT, Smetacek V (1998) Biogeochemical controls and feedbacks on ocean primary production. *Science* 281:200
- Fowler C (2003) Polar Pathfinder Daily 25 km EASE-grid Sea Ice Motion Vectors, 1979–2006. National snow and ice data center, Boulder. Digital media (2003, updated 2008)
- Funke B, López-Puertas M, Gil-López S, von Clarmann T, Stiller GP, Fischer H, Kellmann S (2005) Downward transport of upper atmospheric NO_x into the polar stratosphere and lower mesosphere during the Antarctic 2003 and Arctic 2002/2003 winters. *J Geophys Res* 110:D24308
- Funke B, Baumgaertner A, Calisto M, Egorova T, Jackman CH, Kieser J, Krivolutsky A, López-Puertas M, Marsh DR, Reddmann T, Rozanov E, Salmi S–M, Sinnhuber M, Stiller GP, Verronen PT, Versick S, von Clarmann T, Vyushkova TY, Wieters N, Wissing JM (2011) Composition changes after the “Halloween” solar proton event: the high energy particle precipitation in the atmosphere (HEPPA) model versus MIPAS data intercomparison study. *Atmos Chem Phys* 11:9089–9139
- Gallet J–C, Dominé F, Arnaud L, Picard G, Savarino J (2010) Vertical profiles of the specific surface area of the snow at Dome C, Antarctica. *The Cryosphere Discuss* 4:1647–1708. doi:[10.5194/tcd-4-1647-2010](https://doi.org/10.5194/tcd-4-1647-2010)
- Garcia RR, Marsh DR, Kinnison DE, Boville BA, Sassi F (2007) Simulation of secular trends in the middle atmosphere, 1950–2003. *J Geophys Res* 112:D09301
- Gregg WW, Casey NW (2007) Modeling coccolithophores in the global oceans. *Deep Sea Res Pt. II*, 54(5–7), 447–477
- Haltrin VI (2006) Absorption and scattering of light in natural waters. In: Kokhanovsky AA (ed) *Light scattering reviews*. Springer, Praxis Publishing, Chichester, pp 445–486
- Hoffmann CG, Raffalski U, Palm M, Funke B, Golchert SHW, Hochschild G, Notholt J (2011) Observation of strato-mesospheric CO above Kiruna with ground-based microwave radiometry—retrieval and satellite comparison. *Atmos Meas Tech* 4:2389–2408
- Hoffmann CG, Kinnison DE, Garcia RR, Palm M, Notholt J, Raffalski U, Hochschild G (2012) CO at 40–80 km above Kiruna observed by the ground-based microwave radiometer KIMRA and simulated by the whole atmosphere community climate model. *Atmos Chem Phys* 12:3261–3271

- Holligan PM, Fernandez E, Aiken J, Balch WM, Boyd P, Burkill PH, Finch M, Groom SB, Malin G, Muller K, Purdie DA, Robinson C, Trees CC, Turner SM, Van der Wal P (1993) A biogeochemical study of the coccolithophore *Emiliania huxleyi* in the North Atlantic. *Global Biogeochem Cyc* 7(4):879–900
- Holton JR, Haynes PH, McIntyre ME, Douglass AR, Rood RB, Pfister L (1995) Stratosphere–troposphere exchange. *Rev Geophys* 33:403–439
- Huijnen V, Eskes HJ, Poupkou A, Elbern H, Boersma KF, Foret G, Sofiev M, Valdebenito A, Flemming J, Stein O, Gross A et al (2010) Comparison of OMI NO₂ tropospheric columns with an ensemble of global and European regional air quality models. *Atmos Chem Phys* 10:3273–3296
- Jackman CH, DeLand MT, Labow GJ, Fleming EL, Weisenstein DK, Ko MKW, Sinnhuber M, Russell JM (2005) Neutral atmospheric influences of the solar proton events in October–November 2003. *J Geophys Res* 110:A09S27
- Jacob DJ, Crawford JH, Kleb MM, Connors VS, Bendura RJ, Raper JL, Sachse GW, Gille JC, Emmons L, Heald CL (2003) Transport and chemical evolution over the Pacific (TRACE-P) aircraft mission: design, execution, and first results. *J Geophys Res* 108:9000
- Konovalov IB, Beekmann M, Richter A, Burrows JP, Hilboll A (2010) Multi-annual changes of NO_x emissions in megacity regions: nonlinear trend analysis of satellite measurement based estimates. *Atmos Chem Phys* 10:8481–8498
- Kopelevich OV (1983) Small-parameter model of optical properties of seawater. In: Monin AS (ed) *Ocean optics, physical ocean optics*, vol 1. Nauka, Moscow (in Russian), pp 208–234
- Korb RE, Whitehouse MJ (2004) Contrasting primary production regimes around South Georgia, Southern Ocean: large blooms versus high nutrient, low chlorophyll waters. *Deep-Sea Res I* 51(5). doi:[10.1016/j.dsr.2004.02.006](https://doi.org/10.1016/j.dsr.2004.02.006)
- Lannuzel D, Shoemann V, de Jong J, Tison JL, Chou L (2007) Distribution and biogeochemical behaviour of iron in the East Antarctic sea ice. *Mar Chem* 106. doi:[10.1016/j.marchem.2006.06.010](https://doi.org/10.1016/j.marchem.2006.06.010)
- Lary DJ (1997) Catalytic destruction of stratospheric ozone. *J Geophys Res* 102:21515–21526
- Levelt PF, van den Oord GHJ, Dobber MR, Malkki A, Huib Visser H, Johan de Vries G, Stammes P, Lundell JOV, Saari H (2006) The ozone monitoring instrument. *IEEE Trans Geosci Rem Sens* 44:1093–1101
- Longhurst AR (1998) *Ecological geography of the sea*, Academic Press, San Diego, Calif
- López-Puertas M, Funke B, Gil-López S, von Clarmann T, Stiller GP, Höpfner M, Kellmann S, Fischer H, Jackman CH (2005) Observation of NO_x enhancement and ozone depletion in the northern and southern hemispheres after the October–November 2003 solar proton events. *J Geophys Res* 110:A09S43
- Lövblad G, Tarrasón L, Tørseth K, Dutchak S (2004) EMEP assessment part I European perspective. Norwegian Meteorological Institute, Oslo
- Mackey MD, Mackey DJ, Higgins HW, Wright SW (1996) CHEMTAX—a program for estimating class abundances from chemical markers: application to HPLC measurements of phytoplankton. *Mar Ecol Prog Ser* 144:265–283
- Marinov I, Gnanadesikan A, Toggweiler JR, Sarmiento JL (2006) The Southern Ocean biogeochemical divide. *Nature* 441. doi:[10.1038/nature04883](https://doi.org/10.1038/nature04883)
- Milliman JD (1993) Production and accumulation of calcium in the ocean. *Global Biogeochem Cyc* 7:927–957
- Mobley CD (1994) *Light and water. Radiative transfer in natural waters*. Academic Press, San Diego
- Morel A (1974) Optical properties of pure water and pure seawater. In: Jerlov NG, Steemann Nielsen E (eds) *Optical aspects of oceanography*. Academic, New York, pp 1–24
- Morel A, Maritorena S (2001) Bio-optical properties of oceanic waters: a reappraisal. *J Geophys Res* 106(C4):7163–7180
- Mudelsee M (2010) *Climate time series analysis*. Springer, Dordrecht
- Nair A, Sathyendranath S, Platt T, Morales J, Stuart V, Forget M, Devred E, Bouman H (2008) Remote sensing of phytoplankton functional types. *Remote Sens Environ* 112:3366–3375

- Nolin A, Dozier J (2000) A hyperspectral method for remotely sensing the grain size of snow. *Remote Sens Environ* 74:207–216. doi:[10.1016/S0034-4257\(00\)00111-5](https://doi.org/10.1016/S0034-4257(00)00111-5)
- Nüß JH (2005) Improvements of the retrieval of tropospheric NO₂ from GOME and SCIAMACHY data. Ph D thesis, University of Bremen
- O'Reilly JE, Maritorena S, Mitchell BG, Siegel DA, Carder KL, Garver SA, Kahru M, McClain C (1998) Color chlorophyll algorithms for SeaWiFS. *J Geophys Res* 103(C11):24937–24953
- Painter T, Molotch N, Cassidy M, Flanner M, Steffen K (2007) Contact spectroscopy for determination of stratigraphy of snow optical grain size. *J Glaciol* 53:121–127. doi:[10.3189/172756507781833947](https://doi.org/10.3189/172756507781833947)
- Park J, Oh I-S, Kim H-C, Yoo S (2010) Variability of SeaWiFS chlorophyll-a in the southwest Atlantic sector of the Southern Ocean: strong topographic effects and weak seasonality. *Deep-Sea Res I* 57. doi:[10.1016/j.dsr.2010.01.004](https://doi.org/10.1016/j.dsr.2010.01.004)
- Parkinson CL, Cavalieri DJ (2002) A 21 year record of Antarctic sea-ice extents and their regional, seasonal and monthly variability and trends. *Ann Glac* 34:441–446
- Perner D, Platt U (1979) Detection of nitrous acid in the atmosphere by differential optical absorption. *Geophys Res Lett* 93:917–920
- Platt U, Stutz J (2008) *Differential optical absorption spectroscopy*. Springer, Berlin
- Pope RM, Fry ES (1994) Absorption spectrum (380–700 nm) of pure water. II. Integrating cavity measurements. *Appl Optics* 36(33):8710–8723
- Porter HS, Jackman CH, Green AES (1976) Efficiencies for production of atomic nitrogen and oxygen by relativistic proton impact in air. *J Chem Phys* 65:154–167
- Powell MJD (1964) An efficient method for finding the minimum of a function of several variables without calculating derivatives. *Comput J* 7(2):155–162
- Prieur L, Sathyendranath S (1981) An optical classification of coastal and oceanic waters based on the specific absorption curves of phytoplankton pigments, dissolved organic matter, and other particulate materials. *Limnol Oceanogr* 26:671–689
- Raitsos DE, Lavender SJ, Pradhan Y, Tyrrell T, Reid PC, Edwards M (2006) Coccolithophore bloom size variation in response to the regional environment of the subarctic North Atlantic. *Limnol Oceanogr* 51:2122–2130
- Randall D, Wood R, Bony S, Colman R, Fichetef T, Fyfe J, Kattsov V, Pitman A, Shukla J, Srinivasan J, Stoufer R, Sumi A, Taylor K (2007a) Climate models and their evaluation. In: Solomon S, Qin D, Manning M, Chen Z, Marquis M, Averyt K, Tignor M, Miller H (eds) *Climate change 2007: the physical science basis. Contribution of working group I to the fourth assessment report of the intergovernmental panel on climate change*. Cambridge University Press, Cambridge
- Randall CE, Harvey VL, Singleton CS, Bailey SM, Bernath PF, Codrescu M, Nakajima H, Russell JM III (2007b) Energetic particle precipitation effects on the Southern hemisphere stratosphere in 1992–2005. *J Geophys Res* 112:D08308
- Randall CE, Harvey VL, Siskind DE, France J, Bernath PF, Boone CD, Walker KA (2009) NO_x descent in the Arctic middle atmosphere in early 2009. *Geophys Res Lett* 36:L18811
- Rao KN, Weber A (1992) *Spectroscopy of the Earth's atmosphere and interstellar medium*. Academic Press, Boston
- Richter A, Burrows JP, Nusz H, Granier C, Niemeier U (2005) Increase in tropospheric nitrogen dioxide over China observed from space. *Nature* 437:129–132
- Ridder T, Gerbig C, Notholt J, Rex M, Schrems O, Warneke T, Zhang L (2011) Ship-borne FTIR measurements of CO and O₃ in the western pacific from 43°N to 35°S: an evaluation of the sources. *Atmos Chem Phys* 12:815–828
- Röttgers R, Haese C, Dörffer R (2007) Determination of the particulate absorption of microalgae using a point-source integrating-cavity absorption meter: verification with a photometric technique, improvements for pigment bleaching, and correction for chl. fluorescence. *Limnol Oceanogr Methods* 5:1–12
- Rozanov A (2008) *SCIATRAN 2.X: radiative transfer model and retrieval software package*. URL = <http://www.iup.physik.uni-bremen.de/sciatran>

- Rozanov VV, Buchwitz M, Eichmann K-U, de Beek R, Burrows JP (2002) SciATRAN—a new radiative transfer model for geophysical applications in the 240–2400 nm spectral region: the pseudo-spherical version. *Adv Space Res* 29:1831–1835
- Rozanov A, Rozanov VV, Buchwitz M, Kokhanovsky A, Burrows JP (2005) SCIATRAN 2.0—a new radiative transfer model for geophysical applications in the 175–2400 nm spectral region. *Adv Space Res* 36:1015–1019
- Rusch DW, Gerard JC, Solomon S, Crutzen PJ, Reid GC (1981) The effect of particle precipitation events on the neutral and ion chemistry of the middle atmosphere—I Odd nitrogen. *Planet Space Sci* 29:767–774
- Sarmiento JL, Gruber N (2006) *Ocean biogeochemical dynamics*. Princeton University Press, Princeton
- Sathyendranath S, Watts L, Devred E, Platt T, Caverhill C, Maass H (2004) Discrimination of diatoms from other phytoplankton using ocean-colour data. *Mar Ecol Prog Ser* 272:59–68
- Scambos T, Haran T, Fahnestock M, Painter T, Bohlander J (2007) MODIS-based mosaic of Antarctica (MOA) data sets: continent-wide surface morphology and snow grain size. *Remote Sens Environ* 111:242–257. doi:[10.1016/j.rse.2006.12.020](https://doi.org/10.1016/j.rse.2006.12.020)
- Schlitzer R (2002) Carbon export fluxes in the Southern Ocean: results from inverse modeling and comparison with satellite-based estimates, *Deep-Sea Res II* 49. doi:[10.1016/S0967-0645\(02\)00004-8](https://doi.org/10.1016/S0967-0645(02)00004-8)
- Schwegmann S, Haas C, Fowler C, Gerdes R (2011) A comparison of satellite-derived sea-ice motion with drifting-buoy data in the Weddell Sea, Antarctica. *Ann Glac* 52(57):103–110
- Seinfeld JH, Pandis SN (2006) *Atmospheric chemistry and physics: from air pollution to climate change*. 2nd edn. Wiley, Hoboken
- Seppälä A, Verronen PT, Kyrölä E, Hassinen S, Backman L, Hauchecorne A, Bertaux JL, Fussen D (2004) Solar proton events of October–November 2003: ozone depletion in the northern hemisphere polar winter as seen by GOMOS/Envisat. *Geophys Res Lett* 31:L19107
- Shchepetkin AF, McWilliams JC (2005) The regional oceanic modeling system (ROMS): a split-explicit, free-surface, topography-following-coordinate oceanic model. *Ocean Mod* 9. doi:[10.1016/j.ocemod.2004.08.002](https://doi.org/10.1016/j.ocemod.2004.08.002)
- Shifrin KS (1988) *Physical optics of ocean water*. AIP translation series. Amer Inst Phys N Y 285
- Sinnhuber B-M, Weber M, Amankwah A, Burrows JP (2003a) Total ozone during the unusual Antarctic winter of 2002. *Geophys Res Lett* 30(11):1580–1584
- Sinnhuber M, Burrows JP, Chipperfield MP, Jackman CH, Kallenrode M-B, Künzi KF, Quack M (2003b) A model study of the impact of magnetic field structure on atmospheric composition during solar proton events. *Geophys Res Lett* 30:1818–1821
- Sinnhuber B-M, Weber M, Amankwah A, Burrows JP (2003c) Total ozone during the unusual Antarctic winter of 2002. *Geophys Res Lett* 30:1580–1583
- Sinnhuber M, Kazeminejad S, Wissing JM (2011) Interannual variation of NO_x from the lower thermosphere to the upper stratosphere in the years 1991–2005. *J Geophys Res* 116:A02312
- Smith KR (1993) Fuel combustion, air pollution exposure, and health: the situation in developing countries. *Annu Rev Energy Environ* 18:529–566
- Solomon S, Rusch D, Gerard J, Reid G, Crutzen P (1981) The effect of particle-precipitation events on the neutral and ion chemistry of the middle atmosphere—2 Odd hydrogen. *Planet Space Sci* 29:885–892
- Solomon S, Garcia RR, Olivero JJ, Bevilacqua RM, Schwartz PR, Clancy RT, Muhleman DO (1985) Photochemistry and transport of carbon monoxide in the middle atmosphere. *J Atmos Sci* 42:1072–1083
- Solomon S, Qin D, Manning M, Chen Z, Marquis M, Averyt KB, Tignor M, Miller HL (2007) Contribution of working group I to the fourth assessment report of the intergovernmental panel on climate change. Cambridge University Press, Cambridge
- Stamnes K, Li W, Eide H, Aoki T, Hori M, Storvold R (2007) ADEOSII/GLI snow/ice products—part I: scientific basis. *Remote Sens Environ* 111:258–273. doi:[10.1016/j.rse.2007.03.023](https://doi.org/10.1016/j.rse.2007.03.023)

- Stroeve JC, Serreze MC, Fetterer F, Arbetter T, Meier W, Maslanik J, Knowles K (2005) Tracking the Arctic's shrinking ice cover: another extreme September minimum in 2004. *Geophys Res Lett* 32. doi:[10.1029/2004GL021810](https://doi.org/10.1029/2004GL021810)
- Swider W, Keneshea TJ (1973) Decrease of ozone and atomic oxygen in lower mesosphere during a PCA event. *Planet Space Sci* 21:1969–1973
- Tagliabue A, Bopp L, Aumont O (2009) Evaluating the importance of atmospheric and sedimentary iron sources to Southern Ocean biogeochemistry. *Geophys Res Lett* 36. doi:[10.1029/2009GL038914](https://doi.org/10.1029/2009GL038914)
- Thompson DWJ, Solomon S (2002) Interpretation of recent Southern hemisphere climate change. *Science* 296:895–899
- Timmermann R, Danilov S, Schröter J, Böning C, Sidorenko D, Rollenhagen K (2009) Ocean circulation and sea ice distribution in a finite element global sea ice-ocean model. *Ocean Model*. doi:[10.1016/j.ocemod.2008.10.009](https://doi.org/10.1016/j.ocemod.2008.10.009)
- Tyrrell T, Holligan PM, Mobley CD (1999) Optical impacts of oceanic coccolithophore blooms. *J Geophys Res* 104(C2):3223–3241
- U.S. Geological Survey: Global Digital Elevation Model (GTOPO30) (2004)
- United Nations Department of Economic and Social Affairs (2010) World urbanization prospects—the 2009 revision: highlights. United Nations Department of Economic and Social Affairs, New York
- van der ARJ, Eskes HJ, Boersma KF, van Noije TPC, Roozendaal MV, Smedt ID, Peters DHMU, Meijer EW (2008) Trends, seasonal variability and dominant NO_x source derived from a ten year record of NO₂ measured from space. *J Geophys Res* 113:D04302
- Verronen PT, Funke B, López-Puertas M, Stiller GP, von Clarmann T, Glatthor N, Enell C-F, Turunen E, Tamminen J (2008) About the increase of HNO₃ in the stratopause region during the Halloween 2003 solar proton event. *Geophys Res Lett* 35:L20809
- Vountas M, Dinter T, Bracher A, Burrows JP, Sierk B (2007) Spectral studies of ocean water with space-borne sensor SCIAMACHY using differential optical absorption spectroscopy (DOAS). *Ocean Sci* 3:429–440
- Wang P, Stammes P, van der AR, Pinardi G, van Roozendaal M (2008) FRESCO+: an improved O₂ A-band cloud retrieval algorithm for tropospheric trace gas retrievals. *Atmos Chem Phys* 8:6565–6576
- Westbroek P, De Vring-De Jong EW, Van Der Wal P, Borman AH, De Vring JPM (1985) Biopolymer-mediated Ca and Mn accumulation and biomineralization. *Geol Mijnbouw* 64:5–15
- Wiebe H (2011) Implementation and validation of the snow grain size retrieval SGSP from spectral reflectances of the satellite sensor MODIS. Ph D thesis, p 106
- Wiebe H, Heygster G, Zege E (2011) Snow grain size retrieval SGSP from optical satellite data: validation with ground measurements and detection of snow fall events. *Rem Sens Environ* (in press)
- Winder M, Cloernet JE (2010) The annual cycles of phytoplankton biomass. *Phil Trans R Soc* 365:3215–3226
- Winkler H, Sinnhuber M, Notholt J, Kallenrode M-B, Steinhilber F, Vogt J, Zieger B, Glassmeier K-H, Stadelmann A (2008) Modeling impacts of geomagnetic field variations on middle atmospheric ozone responses to solar proton events on long timescales. *J Geophys Res* 113:D02302
- Winkler H, Kazeminejad S, Sinnhuber M, Kallenrode M-B, Notholt J (2009) Conversion of mesospheric HCl into active chlorine during the solar proton event in July 2000 in the northern polar region. *J Geophys Res* 114:D00I03
- Wissing JM, Kallenrode M-B (2009) Atmospheric Ionization Module Osnabrück (AIMOS): a 3-D model to determine atmospheric ionization by energetic charged particles from different populations. *J Geophys Res* 114:A06104
- Wissing JM, Kallenrode M-B, Wieters N, Winkler H, Sinnhuber M (2010) Atmospheric ionization module Osnabrück (AIMOS): 2. Total particle inventory in the October–November 2003 event and ozone. *J Geophys Res* 115:A02308

- WMO (World Meteorological Organization) (2007) Scientific assessment of ozone depletion: 2006, global ozone research and monitoring project—report no. 50. Geneva
- Yoder JA, McClain CR, Feldman GC, Esaias WE (1993) Annual cycles of phytoplankton chlorophyll concentrations in the global ocean: a satellite view. *Global Biogeochem Cycles* 7(1):181–193
- Zege E, Kokhanovsky A, Katsev I, Polonsky I, Prikhach A (1998) The retrieval of the effective radius of snow grains and control of snow pollution with GLI data. In: Mishchenko M, Travis L, Hovenier J (eds) Proceedings of conference on light scattering by nonspherical particles: theory, measurements, and applications. American Meteorological Society, Boston, pp 288–290
- Zege E, Katsev I, Malinka A, Prikhach A, Polonsky I (2008) New algorithm to retrieve the effective snow grain size and pollution amount from satellite data. *Ann Glaciol* 49:139–144. doi:[10.3189/172756408787815004](https://doi.org/10.3189/172756408787815004)
- Zege EP, Katsev IL, Malinka AV, Prikhach AS, Heygster G, Wiebe H (2011) Algorithm for retrieval of the effective snow grain size and pollution amount from satellite measurements. *Remote Sens Environ* 115(10):2674–2685
- Zhang Q, Streets DG, He K, Wang Y, Richter A, Burrows JP, Uno I, Jang CJ, Chen D, Yao Z, Lei Y (2007) NO_x emission trends for China, 1995–2004: the view from the ground and the view from space. *J Geophys Res* 112:D22306

Earth System Science: Bridging the Gaps between
Disciplines

Perspectives from a Multi-Disciplinary Helmholtz
Research School

Lohmann, G.; Grosfeld, K.; Wolf-Gladrow, D.; Unnithan,
V.; Notholt, J.; Wegner, A. (Eds.)

2013, XI, 134 p. 61 illus., 52 illus. in color., Softcover

ISBN: 978-3-642-32234-1